HHS Public Access

Author manuscript

Cell. Author manuscript; available in PMC 2021 January 09.

Published in final edited form as:

Cell. 2020 January 09; 180(1): 188–204.e22. doi:10.1016/j.cell.2019.11.036.

A Patient-Derived Glioblastoma Organoid Model and Biobank Recapitulates Inter- and Intra-tumoral Heterogeneity

Fadi Jacob[1,2,3,19], **Ryan D. Salinas**[4,19], **Daniel Y. Zhang**[5,19], **Phuong T.T. Nguyen**[6,19], **Jordan G. Schnoll**[1], **Samuel Zheng Hao Wong**[1,7], **Radhika Thokala**[4], **Saad Sheikh**[8], **Deeksha Saxena**[8], **Stefan Prokop**[9,18], **Di-ao Liu**[10], **Xuyu Qian**[1,11], **Dmitriy Petrov**[4], **Timothy Lucas**[4], **H. Isaac Chen**[4,12,13], **Jay F. Dorsey**[9,14], **Kimberly M. Christian**[1], **Zev A. Binder**[4,14], **MacLean Nasrallah**[9,14], **Steven Brem**[4,14], **Donald M. O'Rourke**[4,14,*], **Guo-li Ming**[1,12,15,16,*], **Hongjun Song**[1,12,14,15,17,20,*]

[1]Department of Neuroscience and Mahoney Institute for Neurosciences, University of Pennsylvania, Philadelphia, PA 19104, USA

[2]The Solomon H. Snyder Department of Neuroscience, Johns Hopkins University School of Medicine, Baltimore, MD 21205, USA

[3]Medical Scientist Training Program, Johns Hopkins University School of Medicine, Baltimore, MD 21205, USA

[4]Department of Neurosurgery, University of Pennsylvania, Philadelphia, PA 19104, USA

[5]Biochemistry and Molecular Biophysics Graduate Group, University of Pennsylvania, Philadelphia, PA 19104, USA

[6]Neuroscience Graduate Group, University of Pennsylvania, Philadelphia, PA 19104, USA

[7]Graduate Program in Cellular and Molecular Medicine, Johns Hopkins University School of Medicine, Baltimore, MD 21205, USA

[8]Department of Radiation Oncology, University of Pennsylvania, Philadelphia, PA 19104, USA

[9]Department of Pathology and Laboratory Medicine, University of Pennsylvania, Philadelphia, PA 19104, USA

[*]Correspondence: donald.orourke@pennmedicine.upenn.edu (D.M.O.), ming@pennmedicine.upenn.edu (G.-l.M.), shongjun@pennmedicine.upenn.edu (H.S.).

AUTHOR CONTRIBUTIONS

F.J. developed tissue processing and GBO culture methods, performed immunohistological analyses, CAR-T testing and biobanking, and contributed to culturing and *in vivo* drug testing. R.D.S. developed protocol and coordinated tissue collection, performed *in vitro* drug treatment testing, and contributed to culturing and gene expression analysis. D.Y.Z. performed gene expression and genome sequencing analyses. P.T.T.N. developed and performed xenograft analysis and *in vivo* drug testing. S.Z.H.W. and D.L. contributed to gene expression and genome sequencing library generation and analysis. M.N. performed neuropathological analysis of tumors and GBOs. J.G.S. contributed to immunohistological characterizations. R.T., S.S., D.S, X.Q., H.I.C., J.F.D., K.M.C., and Z.A.B. contributed to additional data collection and analyses. S.P., D.P., T.L., S.B., and D.M.O. contributed to tumor tissue collection. F.J., R.D.S., D.Y.Z., P.T.T.N., G.-l.M., and H.S. conceived the project and wrote the manuscript.

SUPPLEMENTAL INFORMATION

Supplemental Information can be found online at https://doi.org/10.1016/j.cell.2019.11.036.

DECLARATION OF INTERESTS

J.F.D. has ownership interest (including equity, patents, etc.) in Liquid Biotech USA, Inc., and PolyAurum, LLC. The University of Pennsylvania has submitted a patent application based on the EGFRvIII digital PCR assay utilized. Other authors declare no competing interests.

[10]Department of Biology, University of Pennsylvania, Philadelphia, PA 19104, USA

[11]Bioengineering Graduate Program, Johns Hopkins University School of Medicine, Baltimore, MD 21205, USA

[12]Institute for Regenerative Medicine, University of Pennsylvania, Philadelphia, PA 19104, USA

[13]Corporal Michael J. Crescenz Veterans Affairs Medical Center, Philadelphia, PA 19104, USA

[14]Glioblastoma Translational Center of Excellence, The Abramson Cancer Center, University of Pennsylvania, Philadelphia, PA 19104, USA

[15]Department of Cell and Developmental Biology, University of Pennsylvania, Philadelphia, PA 19104, USA

[16]Department of Psychiatry, University of Pennsylvania, Philadelphia, PA 19104, USA

[17]The Epigenetics Institute, Perelman School of Medicine, University of Pennsylvania, Philadelphia, PA 19104, USA

[18]Present address: Department of Pathology, University of Florida, Gainesville, FL 32610, USA

[19]These authors contributed equally

[20]Lead Contact

SUMMARY

Glioblastomas exhibit vast inter- and intra-tumoral heterogeneity, complicating the development of effective therapeutic strategies. Current *in vitro* models are limited in preserving the cellular and mutational diversity of parental tumors and require a prolonged generation time. Here, we report methods for generating and biobanking patient-derived glioblastoma organoids (GBOs) that recapitulate the histological features, cellular diversity, gene expression, and mutational profiles of their corresponding parental tumors. GBOs can be generated quickly with high reliability and exhibit rapid, aggressive infiltration when transplanted into adult rodent brains. We further demonstrate the utility of GBOs to test personalized therapies by correlating GBO mutational profiles with responses to specific drugs and by modeling chimeric antigen receptor T cell immunotherapy. Our studies show that GBOs maintain many key features of glioblastomas and can be rapidly deployed to investigate patient-specific treatment strategies. Additionally, our live biobank establishes a rich resource for basic and translational glioblastoma research.

Graphical Abstract

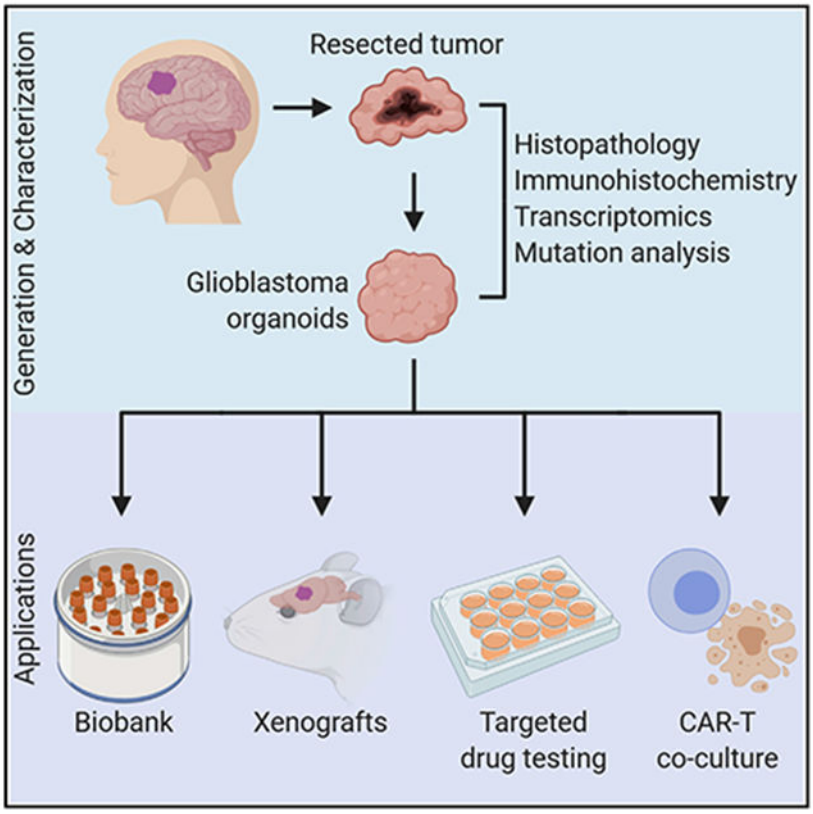

In Brief

A rapid and reliable method to generate patient-derived glioblastoma organoids captures the features and diversity of their respective parental tumors to allow for testing personalized therapies correlated to organoid profile and the establishment of a biobank for further basic and translational glioblastoma research.

INTRODUCTION

Glioblastoma is the most prevalent primary malignant brain tumor in adults (Ostrom et al., 2018) and remains almost invariably lethal due to its aggressive and invasive nature. Despite many clinical trials (Paolillo et al., 2018), the standard of care therapy for over a decade has been maximal surgical resection followed by temozolomide chemotherapy and radiation treatment, which improves the median survival duration to 14.6 months when compared to 12.1 months with surgery and radiation alone (Stupp et al., 2005). It has been increasingly appreciated that molecular heterogeneity among tumors (Brennan et al., 2013) and within tumors (Darmanis et al., 2017; Neftel et al., 2019; Patel et al., 2014) likely contributes to poor outcomes of numerous clinical trials (Mandel et al., 2018). Characterizing this heterogeneity and developing new models for timely empirical testing of personalized treatment strategies for glioblastoma remain both pre-clinical and clinical challenges.

Several model systems have contributed tremendously to our current understanding of biological mechanisms underlying glioblastoma pathogenesis, but have their limitations.

Traditional *in vitro* culture models, both monolayer and tumor sphere cultures, can require a substantial amount of time to establish and use exogenous EGF, bFGF, and/or serum to propagate tumor cells over serial passages with clonal expansion, which are not favorable to maintain various cellular subtypes and key driver gene expression of parental tumors (Ledur et al., 2017; Lee et al., 2006). Patient-derived xenograft (PDX) models, in which primary dissociated tumor cells are directly injected into mice, are thought to better retain these important features of glioblastomas (Giannini et al., 2005). However, these PDX models exhibit variable engraftment efficiency and host infiltration by tumor cells, have very limited throughput, and are subject to a long latency in tumor generation ranging from 2 to 11 months (Patrizii et al., 2018). The protracted time required to establish clonal tumor cell cultures and PDX models hinders their clinical applicability for testing personalized therapy as current treatment regimens are typically initiated 1 month following surgery, and the median survival time of patients upon diagnosis is 14.6 months.

Recently, 3D organoid culture systems have been developed that capture the phenotypic and molecular heterogeneity found in various organs (Clevers, 2016), including cerebral organoids (Kadoshima et al., 2013; Lancaster et al., 2013; Paşca et al., 2015; Qian et al., 2016). Organoids have since been applied to model various cancers, including pancreatic, prostate, liver, breast, bladder, ovarian, and gastrointestinal cancers (Boj et al., 2015; Broutier et al., 2017; Gao et al., 2014; Kopper et al., 2019; Lee et al., 2018; Sachs et al., 2018; Yan et al., 2018). In most cases, dissociated tumor cells of epithelial origin are cultured within Matrigel in the presence of exogenous growth factors to form 3D structures, and various cancer organoid biobanks have been established as valuable resources (Bleijs et al., 2019). To study glioblastoma, cerebral organoids have been genetically manipulated to develop oncogenic properties (Bian et al., 2018; Ogawa et al., 2018) or co-cultured with tumor spheres to model tumor cell invasion (da Silva et al., 2018; Linkous et al., 2019). Furthermore, patient-derived glioblastoma organoids generated with Matrigel and exogenous EGF/bFGF over several weeks have demonstrated stem cell heterogeneity and a hypoxic gradient (Hubert et al., 2016). The degree to which these glioblastoma organoid systems recapitulate key molecular features of patient tumors remains unclear.

Here, we report a robust method to rapidly generate glioblastoma organoids (named GBOs) in a defined culture medium directly from fresh tumor specimens without single-cell dissociation. We generated a live biobank of GBOs and performed comprehensive histological, molecular, and genomic analyses to show that GBOs recapitulate inter- and intra-tumoral heterogeneity and retain many key features of their corresponding parental tumors. These GBOs can be efficiently xenografted into the adult mouse brain, displaying rapid and aggressive infiltration and maintaining key driver mutation expression. We further show that GBOs can be employed to test responses to standard of care therapy as well as targeted treatments, including drugs from clinical trials and chimeric antigen receptor T (CAR-T) cell immunotherapy, on a clinically relevant timescale. Together, these results highlight the potential utility of our patient-derived glioblastoma organoid model and biobank for basic and translational research and for testing personalized therapies.

RESULTS

Culture and Banking of Glioblastoma Organoids from Patient Tumors

To preserve the local cytoarchitecture and native cell-cell interactions of original tumors, and to avoid clonal selection of specific cell populations in culture, we developed a protocol to generate glioblastoma organoids (GBOs) without mechanical or enzymatic dissociation of the resected tumor tissue into single cells (Figure 1A). Furthermore, the optimized medium to establish and maintain GBOs is fully defined, serum-free, and with no added EGF/bFGF or extracellular matrix that may contribute to further selection. We obtained fresh surgically resected glioblastoma tumor tissue from patients after informed consent (Table S1). Optimal GBOs were generated from tissue along the tumor margin with minimal necrosis and little surrounding brain tissue. The resected tissue was cut into ~1 mm diameter pieces using fine dissection scissors (Figure 1A). Debris and red blood cells were removed and tumor pieces were cultured in the GBO medium on an orbital shaker to facilitate organoid formation and increase nutrient and oxygen diffusion. Tumor pieces generally formed round organoids within 1–2 weeks (Figure 1A). GBOs were propagated by cutting them into ~0.5 mm diameter pieces to avoid necrotic cell death in the inner core (Figure 1A).

To assess whether GBOs resemble their corresponding parental tumors, we first performed histological analyses. Each GBO was independently confirmed by a neuropathologist to retain features of high-grade gliomas using H&E staining (Figure 1B). These GBOs displayed the cellular and nuclear atypia of patient tumors, often containing abundant mitotic figures and pleomorphic nuclei (Figure 1B). In particular, GBOs exhibited many characteristic cellular morphologies of their parental tumors, such as gemistocytic cells (UP-7966), multinucleated giant cells (UP-8036 and UP-7955), and cells with abundant vacuoles (UP-7884). Many GBOs also retained $CD31^+$ vasculature (Figure 1C). GBOs allowed to grow larger developed hypoxia gradients (Figure 1D), a hallmark of glioblastomas (Hubert et al., 2016). Hypoxia increased substantially around 300 μm from the surface, correlating with absence of $KI67^+$ proliferating cells (Figure 1D).

To further characterize cellular identities, we performed immunohistological analyses using a panel of neurodevelopmental markers, including glial markers GFAP and S100B, immature neuronal marker DCX, and neural progenitor and glioma stem cell markers NESTIN, BLBP, HOPX, SOX2, and OLIG2. We observed robust heterogeneity in cell identity and morphology in GBOs with close resemblance to the cellular composition of corresponding parental tumors, which exhibited marked inter-tumoral heterogeneity (Figures 2A and S1A). Quantitative analysis of 8 tumor samples showed similar percentages of cells expressing SOX2 and OLIG2 between parental tumors and corresponding GBOs for up to 4 weeks in the majority of cases (Figure 2B). GBOs largely maintained the proliferation rate of corresponding parental tumors as quantified by KI67 immunostaining (Figures 2A and 2B). We observed small numbers of dying cells in non-necrotic regions for some parental tumors and derived GBOs, but not for others (Figure S1B). To examine GBO expansion, we pulsed GBOs with 5-ethynyl-2′-deoxyuridine (EdU). At 1 h after labeling, the majority of EdU^+ cells were $NESTIN^+$, $S100B^+$, DCX^+, or $OLIG2^+$, revealing progenitor subtypes that were actively dividing in these GBOs (Figures 2C and 2D). Two weeks later, EdU-retaining

cells included NESTIN$^+$, HOPX$^+$, DCX$^+$, S100B$^+$, OLIG2$^+$, and GFAP$^+$ cells, indicating continuous generation of diverse cell types that were typically present in parental tumors (Figures 2A and 2D). We have also monitored GBO growth by measuring the size of individual GBOs over time (Figures S2A and S2B).

We have generated GBOs with high reliability from glioblastomas of 53 patient cases, including from anatomical subregions of the same tumors and from recurrent tumors (Figure S2C; Table S1). We defined successful GBO generation as microdissected tumor pieces that could survive, develop a spherical morphology, and continuously grow in culture for 2 weeks. Using these criteria, our overall success rate for generating GBOs was 91.4%, with 66.7% for *IDH1* mutant tumors and 75% for recurrent tumors (Table S1). GBOs could be cultured for over 48 weeks and maintained similar expression of markers examined (Figures S2D and S2E). We also developed protocols for freezing cultured GBOs and recovering them from cryopreservation. These recovered GBOs exhibited continuous growth (Figures 2E and 2F) and similar expression of various markers to their corresponding parental tumors (Figures 2A, 2B, S1, and S2D). So far, we have established a biobank of 70 GBOs from 53 patient cases (including subregional samples) carrying a variety of genomic alterations commonly found in glioblastomas (Brennan et al., 2013) (Figure S2F; Table S1) and performed additional characterizations for a subset of these GBOs (Table S2).

Maintenance of Molecular and Mutation Inter- and Intra-tumoral Heterogeneity by GBOs

We next assessed whether GBOs also maintained gene expression signatures and genomic landscapes similar to their corresponding parental tumors. We performed transcriptome analysis by bulk RNA sequencing (RNA-seq) across 12 patients, including 2 patients with subregional samples, for a total of 17 parental tumor samples and 64 derived GBOs in culture for 1 to 12 weeks (Table S3). Overall, transcriptome-wide comparisons of GBOs with their corresponding parental tumors demonstrated high similarity (Figures 3A and S3A). Given the large inter-tumoral heterogeneity for glioblastomas, we identified unique gene expression signatures for individual parental tumors and found that corresponding GBOs maintained these patterns of gene expression in culture over time (Figure 3B). For example, *EGFR* expression was maintained at high levels in UP-7788-ANT-GBOs and at low levels in UP-7790-GBOs, as shown by both RNA-seq and immunohistology (Figures S3B and S3C). Systematic comparison between parental tumors and derived GBOs showed that the major difference was downregulation of blood- and immune-related genes in GBOs (Figures S3D–S3F), likely reflecting the elimination of blood cells and a lack of immune cell expansion in GBOs overtime. Few genes were upregulated in GBOs compared to parental tumors (Figures S3D and S3F).

To determine whether GBOs maintain genomic alterations found in parental tumors, we performed exome sequencing of 13 parental tumor samples, their corresponding GBOs at 2 weeks, and matched blood samples (Table S3). We focused on somatic variants listed in a recent comprehensive study of glioblastoma genomics (Brennan et al., 2013). The majority of somatic variants identified in parental tumors was found in corresponding GBOs at similar allele frequencies (Figure 3C; Table S3). Copy number variants (CNVs) detected in parental tumors were also identified in corresponding GBOs at similar copy number ratios

(Figures 3C and S3G). Notably, inter-tumoral heterogeneity was largely retained in corresponding GBOs (Figure 3C).

To assess the maintenance of intra-tumoral heterogeneity in GBOs, we examined subregion samples. Genomics analyses revealed that subregion-specific genomic variants, such as a *PTEN* missense mutation and copy number loss of 6q and 16q in the UP-7788-PMS subregion, but not in the UP-7788-ANT subregion, were maintained in corresponding GBOs (Figure 3C). Gene expression analysis also showed that GBOs maintained signatures of subregion tumor samples (Figures 3B and 3D). As an example, RNA-seq and digital PCR detected differential expression of the gain-of-function *EGFR* variant III (*EGFRvIII*) in different subregions (ANT and PMS) of the UP-7788 tumor and corresponding GBOs (Figures 3E and 3F), which was further confirmed by immunohistology (Figure 3G).

Together, these results demonstrate that GBOs largely maintain molecular signatures of corresponding parental tumors, including inter- and intra-tumoral transcriptomic and genomic heterogeneity.

Maintenance of Cell-Type Heterogeneity and Molecular Signatures by GBOs

To further investigate cell-type heterogeneity and its molecular signatures, we performed single-cell transcriptome analysis of parental tumors from 3 patients and corresponding GBOs at 2 weeks and later time points, including two subregion samples from 1 patient (Table S4). At the single cell level, neoplastic cells from both parental tumors and derived GBOs, as determined by copy number alteration (CNA) status (Tirosh et al., 2016) and marker gene expression (Figure S4A), exhibited patient-specific clustering, whereas non-neoplastic cell types such as macrophages/microglia, T cells, stromal cells, and myelinating oligodendrocytes from different patients clustered together (Figures 4A and 4B). Macrophage/microglia cells showed similar expression of many immune-related genes in the parental tumors and GBOs at 2 weeks, including cytokines such as *TNF*, *IL1B*, and *TGFB1*, suggesting that certain features of the tumor microenvironment were maintained within GBOs (Figure 4C). Some of these cells exhibited microglia-associated gene signatures and others exhibited macrophage-like gene signatures with an overall enrichment of macrophage-like cell states in culture (Figure 4D). We confirmed the presence of macrophage/microglia and T cells within tumors and derived GBOs by immunohistology for IBA1 and CD3, respectively (Figure 4E). We also performed single-cell RNA-seq for UP-8036-GBOs at 8 weeks and UP-8165 and UP-8167 GBOs at 24 weeks (Table S4). We found similar distributions of cells at later time points as for the parental tumor and corresponding GBOs at 2 weeks (Figures 4F, S4B, and S4G), suggesting the maintenance of cell types and molecular signatures of parental tumors by GBOs over extended time in culture.

Many different cell clusters were identified in parental tumors and corresponding GBOs at 2 weeks (Figures 4G, S4C, and S4H), reflecting the diversity of cell types and cellular states. GBO cell clusters were mapped to the parental tumor cell clusters by pairwise comparisons of whole transcriptome gene expression with a high degree of similarity, indicating that GBOs largely maintain the cellular heterogeneity of parental tumors (Figures 4H, S4D, and S4I). To further explore this heterogeneity, marker genes were identified for each GBO cell

cluster (Table S4). For UP-8036-GBOs, we identified neoplastic populations of proliferating cells, oligodendrocyte precursor cell (OPC)-like, astrocyte-like, oligodendrocyte-like, and neuron-like cells (Figure 4I), similar to results recently reported in primary tumors (Neftel et al., 2019). Comparing their transcriptome profiles to two independent single-nuclei RNA-seq datasets for adult human non-tumor brain cells (Habib et al., 2017; Lake et al., 2018) revealed that these neoplastic cells share similarities with different cell types in the adult human brain (Figure 4J). Similarly, UP-8165 and UP-8167 exhibited multiple populations of neoplastic cells with distinct transcriptomic features in parental tumors and corresponding GBOs (Figures S4E and S4J). Notably, UP-8165-C contained a subregion-specific and distinct population of cells not found in UP-8165-PV in both parental tumors and corresponding GBOs (Figure S4B). This cell population was identified by high expression levels of GPNMB (Figure S4B), which has been linked to worse prognoses in glioblastomas (Kuan et al., 2006).

Together, single-cell RNA-seq analyses highlight marked cellular heterogeneity in GBOs and further support that GBOs recapitulate cell-type heterogeneity and molecular properties of corresponding parental tumors.

Robust Engraftment and Aggressive Infiltration by GBOs upon Xenograft

We next asked whether GBOs reproduce glioblastoma properties *in vivo* with murine xenografts. To minimize the survival bias of different cell types following dissociation and to maintain the integrity and cytoarchitecture of GBOs, we transplanted intact GBOs into adult immunodeficient mouse brains using an established brain organoid transplantation protocol (Mansour et al., 2018) (Figure S5A). We transplanted a total of 8 GBO samples from 7 patients into 5–7 animals for each GBO sample, all of which exhibited engraftment when examined at 1–3 months, indicating a very efficient xenograft model (Table S5).

One major hallmark of glioblastomas is infiltration of tumor cells into the surrounding brain tissue, which is often associated with a FLAIR signal on the patient MRI scan (Kelly et al., 1987) (Figure 5A). At 2 months post-transplantation, analyses of xenografted UP-7788-PMS and UP-7790 GBOs revealed similar tissue architecture at original xenograft sites and infiltrated areas as compared to those of corresponding parental tumors by H&E staining (Figure 5B). We confirmed extensive ipsilateral and contralateral infiltration of GBO-derived cells by immunohistology of human-specific antigens HuNu and STEM121 (Figures 5C–5F). Quantification of infiltrated cells within one brain section of 35 μm thickness showed over 10,000 and 20,200 cells migrated out from original xenograft sites, respectively (Figures 5C and 5E). The majority of infiltrating cells migrated in the white matter, including a subset that crossed the corpus callosum and into the cortex, while a few invaded subcortical areas (Figures 5C and 5E). Reconstruction of the UP-7790 GBO xenograft using serial brain sections showed aggressive tumor growth and infiltration within 3 months (Video S1). Among all xenografted GBOs derived from different tumors, 92% (48 out 52) displayed various degrees of infiltration into the surrounding mouse brain tissue (Table S5). Interestingly, we noted a resemblance of a satellite tumor phenotype in 3 out of 6 UP-7803-GBO xenografted animals and the corresponding original tumor as seen in the patient MRI scan (Figures S5B and S5C). We did not observe such satellite tumor phenotypes in any

other GBO xenografts or patient MRI scans, suggesting maintenance of tumor-specific features in these xenografts.

Consistent with the high angiogenic hallmark of glioblastomas, all xenografted GBOs with the exception of those from one patient were extensively vascularized by host Endoglin$^+$ endothelial cells at 2 months after transplantation (Figures 5D, 5F, and S5D; Table S5). Populations of KI67$^+$ proliferative cells and SOX2$^+$ or NESTIN$^+$ progenitors were found at both initial xenograft sites and distant infiltrated areas (Figures 5D, 5F, and S5D). It has been reported that maintenance of *EGFR* amplification or *EGFRvIII* mutation can be challenging in tumor cell cultures and exogenous overexpression of wild-type *EGFR* or mutant *EGFRvIII* is often required for *in vitro* and *in vivo* modeling (Bigner et al., 1990; Pandita et al., 2004). Importantly, in our model, both *EGFR* amplifications and *EGFRvIII* mutant expression were retained in xenograft sites and infiltrated areas by GBOs derived from *EGFR* amplified and *EGFRvIII*$^+$ tumors (Figures 5D and S5D).

Our xenografts also exhibited rapid infiltration within 1 month *in vivo* (Figure S5E). In addition, GBOs recovered from the biobank were successfully engrafted and exhibited prominent infiltration within 1 month and retained *EGFRvIII* mutant expression (Figure S5E; Table S5).

Taken together, these results demonstrate that orthotopic transplantation of intact GBOs offers a timing advantage over existing PDX models with high efficiency of engraftment, robust infiltration, and retention of key driver mutation expression.

Modeling Targeted Drug Treatments Using GBOs

We next applied our GBO model for testing treatment responses *in vitro*. To mimic the post-surgical standard of care treatment, we subjected 8 GBO samples from 7 patients (Table S6) to a single exposure of 10 Gy radiation with concurrent temozolomide (TMZ, 50 μM) treatment for a week. The therapeutic response was evaluated by quantifying the percentage of cells expressing KI67, which has previously been clinically associated with overall patient survival in treated tumor specimens (Bagley et al., 2019). GBOs from 3 out of 7 patients exhibited decreased percentages of KI67$^+$ cells with temozolomide and radiation treatment (Figures 6A and 6B). One patient (UP-7788) with reduced KI67$^+$ cells in GBOs had a radiographic reduction of tumor volume following treatment of recurrence at 1 month (Figure S6A). Another patient (UP-7884), with reduced KI67$^+$ cells in GBOs from 2 subregions, had no recurrence in the temporal region and exhibited a pattern favoring pseudo-progression in the frontal region (Figure S6B), which has been associated with extended survival (Brandes et al., 2008; Roldán et al., 2009). Meanwhile, 3 patients (UP-7790, UP-7803, and UP-7966) with no significant changes in KI67$^+$ cells in GBOs (Figure 6B) had a below median survival after treatment (1, 3, and 8 months, respectively). Future studies with a larger sample size will be necessary to better establish the correlation between patient and GBO treatment responses. O^6-methylguanine-DNA-methyltransferase (*MGMT*) promoter methylation has been reported to be a predictive marker for response to temozolomide and radiation treatment (Brandes et al., 2008). We did not find a clear association between GBO responses and *MGMT* methylation from this sample set (Figures 6A and 6B). To determine whether the treatment responses had any underlying molecular

basis, we performed gene set enrichment analysis (GSEA) on pre-treated GBO and parental tumor transcriptomes stratified by KI67 responses. The radiation-sensitive group enriched for gene sets associated with response to radiation therapy and tumor necrosis factor (TNF) signaling, while the resistant group enriched for gene sets related to neural stem cells (Figures 6C and S6C; Table S6).

We next explored more targeted drug treatments for specific signaling pathways based on somatic mutations identified in parental tumors from a routinely performed clinical sequencing panel (Figure 6D; Table S1). EGFR tyrosine kinase inhibition did not improve the overall survival of patients with glioblastomas (Rich et al., 2004; Uhm et al., 2011), but showed a survival benefit in patients with mutated *EGFR* in the absence of downstream *PTEN* mutation (Arif et al., 2018; Mellinghoff et al., 2005). We hypothesized that the clinical benefit could be mutation-specific. We therefore treated 10 GBO samples derived from 6 patients with the EGFR inhibitor gefitinib (5 μM) for a week. Reduction of $KI67^+$ cells was observed in 7 GBO samples from 3 patients (Figures 6E and 6F), all of which had *EGFR* alterations (Table S1). These results provide functional evidence suggesting that these *EGFR* alterations drive cell proliferation in these tumors. Two tumors had *EGFR* alterations (UP-7966 with a copy number gain and UP-7803 with clinical detection of *EGFRvIII*) but did not show a reduction of $KI67^+$ cells in GBOs (Figure 6F), indicating that mutation analysis alone without functional testing is not sufficient to predict treatment responses. GSEA for the gefitinib-responders enriched for gene sets associated with EGF signaling and immune-related CCR5 signaling, while the gefitinib-resistant group enriched for gene sets associated with stem cell-associated neural development (Figures 6G and S6D; Table S6).

Mutations downstream of targeted tyrosine kinases are known to contribute to therapeutic resistance (de Bruin et al., 2014; Huang and Fu, 2015). Two tumors had downstream *NF-1* mutations. We therefore tested the MEK inhibitor trametinib (1 μM) to inhibit signaling downstream of NF-1 (Figure 6D). There was a significant reduction of $KI67^+$ cells in *NF-1* mutant GBOs, but not in the *EGFR*-mutated or *PI3K*-mutated GBOs (Figures 6H and 6I). GSEA for *NF1* mutants enriched for gene sets associated with RAS signaling and angiogenesis (Figures 6J and 6K; Table S6), while the *NF1* WT group enriched for a gene set associated with acyl chain remodeling of phosphoinositol, the target of PI3K (Figure 6N), and glutathione conjugation (Figure S6E; Table S6), which is associated with drug resistance (Backos et al., 2012). We next tested the effect of inhibiting PI3K-induced mTOR activation for *NF1* WT tumors (Figure 6D). Everolimus is an mTOR inhibitor with known brain penetration and is currently used to treat subependymal giant cell astrocytoma (Krueger et al., 2010). Treatment with everolimus (1 μM) in UP-7803-GBOs, which had a *PI3K* mutation, exhibited a near complete reduction of $KI67^+$ cells (Figures 6L and 6M). Meanwhile, treatment of UP-8017-GBOs, which had an *EGFR* alteration upstream to both the RAS and PI3K pathways, had a partial reduction of $KI67^+$ cells (Figure 6M). In contrast, UP-7790-GBOs, which had a mutation in the parallel RAS pathway, did not show any reduction (Figures 6L and 6M). The dichotomous treatment effect between PI3K and RAS pathway mutations was further explored with measurement of individual GBO growth. Following an initial 1 week of drug exposure and subsequent 2 weeks in the normal GBO media, mutation-specific resistance and treatment response were also observed when measuring GBO size over time (Figures S6F and S6G). Dose-response analysis with

trametinib exposure to UP-7790-GBOs demonstrated growth inhibition at ~100 nM, while everolimus exposure diminished the size of UP-7803-GBOsat ~10 nM (Figure S6FH). We further confirmed the *in vivo* efficacy of trametinib treatment on reducing tumor cell proliferation upon transplantation of UP-7790-GBOs recovered from the biobank into the adult immunodeficient mouse brain (Figures S6I–S6K).

Together, these results show that responses of GBOs derived from different tumors to various drug treatments are heterogeneous, and the efficacy of targeted treatments is largely consistent with the mutational status and pathway enrichment in tumors. These results demonstrate the value of GBOs for rapid, functional testing of personalized drug treatment responses.

Modeling Personalized CAR-T Immunotherapy Using GBOs

Despite success in many blood cancers (June et al., 2018), CAR-T cell immunotherapy in solid tumors has not been as effective and remains to be further developed (Newick et al., 2017). Recently, the EGFRvIII variant commonly found in glioblastomas has been targeted by CAR-T cells in clinical trials (Goff et al., 2019; O'Rourke et al., 2017). Despite the ability of these EGFRvIII-specific CAR-T cells to penetrate tumors, treatment efficacy was unclear. Current *in vitro* models testing CAR-T cell therapy for glioblastomas generally lack the cellular heterogeneity and maintenance of specific mutant antigens, such as EGFRvIII, in prolonged cultures and often rely on overexpression of antigens in tumor cells for testing (Johnson et al., 2015). To assess the utility of our GBO model, which maintains cellular heterogeneity and endogenous EGFRvIII expression, in testing emerging immunotherapies in glioblastomas, we co-cultured GBOs with 2173BBz CAR-T cells designed to react specifically with cells expressing EGFRvIII (O'Rourke et al., 2017). CAR-T cells targeting CD19 for the B cell blood lineage were used as a control (Porter et al., 2011). We tested CAR-T cell co-cultures with 6 GBO samples, including GBOs containing high (UP-8036) and low (UP-8017) percentages of $EGFRvIII^+$ cells and two pairs of GBOs from subregional sampling of tumors in which one subregion contained a high percentage of $EGFRvIII^+$ cells (UP-7788-PMS and UP-7884-F) and the other subregion did not (UP-7788-ANT and UP-7884-T) as confirmed by immunostaining (Figures 7A and S7A). GBOs were analyzed at 0, 24, and 72 h after CAR-T cell addition for invasion and proliferation of T cells, tumor cell death, and EGFRvIII antigen loss. Both CD19 and 2173BBz CAR-T cells invaded all GBOs, but marked expansion of CAR-T cells was observed only when 2173BBz CAR-T cells were incubated with $EGFRvIII^+$ GBOs (Figures 7A and S7A). This was evidenced by an increased presence of $CD3^+$T cells, many of which were $KI67^+$ within GBOs (Figures 7B and S7B). This increased CAR-T cell expansion was accompanied by increased cleaved-caspase-3 signal and a decreased ratio of EGFRvIII/EGFR signal intensity in GBOs (Figures 7A, 7C, and 7D), suggesting that $EGFRvIII^+$ cells were being targeted and killed by 2173BBz CAR-T cells. To further support this notion, immunostaining for granzyme B, an effector of T cell killing (Shi et al., 2000), revealed T cells filled with granules near apoptotic $EGFRvIII^+$ cells (Figure S7C). These granules often localized on the side of the T cell closest to the $EGFRvIII^+$ tumor cell. ELISA for cytokines interleukin (IL)-2, TNF-α, and interferon (IFN)-γ revealed increases in their levels only in conditions where 2173BBz CAR-T cells were incubated with $EGFRvIII^+$ GBOs, suggesting antigen recognition and

subsequent T cell activation (Figure S7D). Many $EGFR^{+}$ $EGFRvIII^{-}$ tumor cells persisted after 3 days (Figures 7A and S7A), suggesting that the 2173Bbz CAR-T cells are fairly specific to their target and are unable to completely eradicate all tumor cells under our conditions. Together, these results demonstrate the utility of GBOs for rapid testing of antigen-specific CAR-T cell treatment responses with the endogenous target in culture.

DISCUSSION

In contrast to previously reported cancer organoids that have been generated from dissociated tumor cells mostly of epithelial origin with added mitogens and Matrigel, our GBOs retain native cell-cell interactions and are cultured in a defined medium without exogenous EGF/bFGF or extracellular matrix. These GBOs recapitulate the heterogeneity of their corresponding parental tumors as evidenced by (1) histology illustrating similar tissue architecture and cellular morphologies, (2) immunohistology displaying the presence and continual generation of a similar spectrum of diverse cell types, (3) RNA-seq showing maintenance of similar transcriptomic signatures, (4) whole-exome sequencing confirming the preservation of somatic variants and CNVs at similar frequencies, and (5) single-cell RNA-seq revealing the maintenance of different cell populations and their gene expression profiles. Additionally, many GBOs recapitulate specific elements of the tumor microenvironment, such as hypoxia gradients, microvasculature, and immune cell populations. By orthotopic transplantation of intact GBOs into mice, our xenografts displayed efficient engraftment with rapid and aggressive infiltration. We further demonstrate the utility of GBOs by showing that drug treatments and engineered CAR-T cells elicit differential responses depending on tumor-specific mutations. Our robust and rapid method for GBO generation with sufficient throughput for targeted testing makes it possible to accelerate personalized medicine efforts and influence clinical decisions. We have also generated a live biobank of GBOs with diverse mutational profiles as a resource for due future biological studies and therapeutic testing.

A Live Culture and Biobank of Organoids Recapitulating Heterogeneity of Patient Tumors

One important feature of our organoid generation method is that by avoiding single-cell dissociation, we preserve native cell-cell interactions to enable GBO formation and expansion in the absence of exogenous EGF/bFGF, serum and extracellular matrix, which may help GBOs maintain properties similar to the parental tumors. The use of a fully defined culture medium enhances the reproducibility of cultures (Gjorevski et al., 2016) and facilitates its use in future clinical applications. Our GBOs maintain relatively similar proportions of actively proliferating cells as the corresponding parental tumors. Traditional tumor cultures clonally select for highly proliferative cells in growth factor-rich media, reducing the proportion of the more slowly proliferating and non-proliferating cells originally present within parental tumors. These populations may play an important role in glioblastoma pathogenesis and treatment resistance.

Organoid biobanks have been previously established for a number of cancers, including pancreatic, liver, prostate, breast, bladder, ovarian, and gastrointestinal cancers, but not yet for glioblastomas (Bleijs et al., 2019). We provide a resource of 70 biobanked GBOs from

different patients that captures major genomic alterations associated with glioblastoma pathogenesis (Figure S2; Table S1). Our optimized freeze-and-thaw methods allow efficient recovery and continuous growth of GBOs that maintain their resemblance to parental tumors and can efficiently engraft and rapidly infiltrate upon transplantation into the adult mouse brain. We provide detailed characterization for many of these biobanked GBOs, including histology, RNA-seq, whole-exome sequencing, and responses to different drugs and CAR-T therapies (Table S2). As tumor collection and GBO generation is ongoing, this biobank will be a useful resource for future biological studies and testing therapeutics for glioblastomas.

Clinically Relevant Timing

Given the short survival period after diagnosis for the majority of glioblastoma patients, the timing of testing personalized treatment strategies is critical. Compared to the variable efficacy and prolonged generation time for tumor cell lines and PDX models, our methodology is robust for generating patient-derived GBOs from a wide range of glioblastomas within 1–2 weeks from the initial surgical resection. This provides a timely platform with sufficient throughput to test personalized treatment strategies based on individual patient tumor characteristics. Future studies can test the effectiveness of several therapeutic strategies with GBOs from multiple tumor subregions before treatment initiation. Given the heterogeneity of glioblastomas, *in vitro* testing of various therapeutic options may also help refine patient enrollment in clinical trials. Our GBO transplantation model exhibits rapid and aggressive infiltration phenotypes within one month and can be used to test *in vivo* treatment responses in a timely fashion.

Practical Limitations and Future Applications

While our GBOs resemble many features of their corresponding tumors, the model is not without its limitations. Optimal tumor tissue acquisition relies on close coordination with the neurosurgeon intra-operatively to ensure that viable tissue is resected *en bloc* without cauterization. Close coordination with neuropathology is also important to confirm the diagnosis and limit the time span between resection and tissue processing, which is critical for maximum reliability of GBO generation. Our ability to maintain and expand GBOs over very long periods has been variable, likely owing to both tissue quality and the diverse composition and growth characteristics of tumors themselves. In keeping with its more aggressive growth phenotype, the vast majority (96.4%) of *IDH1*-WT tumors have resulted in plentiful GBOs, but our limited experience with *IDH1* mutant tumors and recurrent tumors showed reduced success rates (66.7% and 75.0%, respectively). Further optimization is likely required to establish and propagate these cultures more efficiently. Likewise, our methodology could be adapted and optimized to culture organoids from other brain tumors, such as medulloblastoma or ependymoma. Routine in-depth characterization of all tumors and GBOs as described in this study may be challenging due to the variation in the initial tumor volume obtained and GBO expansion rate, but ample tissue is usually available for basic characterization and testing targeted therapies.

We report the partial preservation of microvasculature and immune cells in some GBOs, which may prove useful in better understanding the tumor microenvironment. However, we found evidence of divergence from primary tumors over time with a decreased abundance of

vasculature and macrophage/microglia populations and lower expression of immune-related genes in GBOs. This is not unexpected as our culture conditions were optimized to preserve tumor cell viability and growth, and resident immune cells have a limited lifespan and become diluted without expansion. Future studies involving the immune microenvironment would ideally be performed early after GBO establishment or after exogenous immune cell reconstitution (Neal et al., 2018). Given the differential proliferation and death of different cell populations in GBOs, the composition of cell types could also drift overtime and it will be best to analyze soon after GBOs are established.

Access to ongoing cultures of live glioblastoma tissue that resemble the parental tumor provides a unique avenue for many future applications. Viral barcoding labeling can be used to trace the division behavior and clonal lineage of specific cell subtypes within GBOs, which can be combined with single-cell RNA-seq and bioinformatic approaches to infer lineage trajectories. Our system should also enable the study of genetic and transcriptional alterations by CRISPR-Cas9 genome editing, small interfering RNA (siRNA) knockdowns, and overexpression vectors, to gain mechanistic insight into glioblastoma pathogenesis. Our platform for drug testing may lead to new therapeutic strategies. Our 3D GBO model additionally provides a platform to test and optimize CAR-T therapies for solid tumors *in vitro* before *in vivo* testing. Importantly, our GBOs recapitulate the endogenous expression of antigens, allowing for a more accurate assessment of CAR-T cell target reactivity, threshold for responses, and specificity, as compared to models engineered to overexpress specific antigens. Therapeutic testing can be extended to GBO xenografts, which recapitulate tumor infiltration into the surrounding brain tissue. The effects of specific drugs, immunotherapy, and/or radiation treatments on GBO composition and regrowth capacity may provide insight into treatment-resistant and recurrence-initiating tumor cell populations. Moreover, matched primary and recurrent parental/GBO pairs may provide additional insight into more invasive and treatment-resistant tumor cell populations.

In summary, our patient-derived GBO model recapitulates the heterogeneity and key features of glioblastomas and has the potential for timely testing of personalized treatment responses and broad applications in basic and translational research of glioblastomas.

STAR★METHODS

LEAD CONTACT AND MATERIALS AVAILABILITY

Further information and requests for resources and reagents should be directed to and will be fulfilled by the Lead Contact, Hongjun Song (shongjun@pennmedicine.upenn.edu). There are restrictions to the availability of biobanked glioblastoma organoids due to the lack of an external centralized repository for their distribution and our need to maintain the stock; however, biobanked organoids generated in this study will be made available upon reasonable request following approval by an internal review board and completion of a Materials Transfer Agreement.

EXPERIMENTAL MODEL AND SUBJECT DETAILS

Human Subjects—The use of human brain tissue and peripheral blood samples was coordinated by the University of Pennsylvania Tumor Tissue/Biospecimen Bank following ethical and technical guidelines on the use of human samples for biomedical research purposes. Patient glioblastoma tissue and peripheral blood samples were collected at the Hospital of the University of Pennsylvania after informed patient consent under a protocol approved by the University of Pennsylvania's Institutional Review Board. All patient samples were de-identified before processing. A total of 58 patient cases (including recurrent cases) from both male and female subjects between the ages of 21-90 years old were included in the present study. Table S1 summarizes detailed epidemiological data for each subject and histological data for each tumor provided by the Neurosurgery Clinical Research Division (NCRD) at the University of Pennsylvania, and testing results for a panel of disease-associated genomic alterations (Agilent Haloplex assay, Illumina HiSeq2500), fusion transcripts (Illumina HiSeq2500), and MGMT promoter methylation (PyroMark Q24, QIAGEN) provided by the University of Pennsylvania Center for Personalized Diagnostics.

Animal Models—All animal procedures used in this study were performed in accordance with protocols approved by the Institutional Animal Care and Use Committee of the University of Pennsylvania. Animals were housed at a maximum of five per cage with a 14-hour light/10-hour dark cycle with food and water *ad libitum*. Female 4-8-week-old athymic nude (NU/J) mice (The Jackson Laboratory, RRID: IMSR_JAX:002019) were used for all experiments and were randomly assigned to treatment groups. Animals were monitored at a minimum of twice weekly for weight loss and were examined routinely for physical and/or neurological abnormalities.

METHOD DETAILS

Collection, Dissection, and Processing of Patient Glioblastoma Samples—Fresh surgically resected glioblastoma tissue was placed in sterile phosphate buffered saline and taken immediately to the University of Pennsylvania Department of Pathology to confirm a preliminary diagnosis of high-grade glioma by the attending neuropathologist (M.N.). In cases where a large amount of *en bloc* tissue was available, the tissue was sub-divided into anatomically distinct subregions for analysis of intra-tumoral heterogeneity. After preliminary diagnosis of glioblastoma was confirmed, the tissue was distributed and placed in Hibernate A medium (BrainBits) kept at 4°C. For reliable organoid generation it was imperative that the tissue was processed immediately as a prolonged time between surgical removal and tissue processing reduced the reliability of GBO generation. The tissue was transferred to a sterile glass dish with H+GPSA medium containing Hibernate A, 1X GlutaMax (Thermo Fisher Scientific), 1X PenStrep (Thermo Fisher Scientific), and 1X Amphotericin B (Thermo Fisher Scientific) for dissection under a stereomicroscope (Zeiss) within a laminar flow biosafety cabinet. The amount of glioblastoma tissue received ranged from 0.5 to 2 mL in volume. The resected tumors were minced into approximately 0.5 to 1 mm diameter pieces using fine dissection scissors (Fine Science Tools) and washed with H +GPSA medium to remove cellular debris. Pieces containing substantial amounts of necrosis or surrounding brain tissue were removed. Tumor pieces were incubated in 1X RBC lysis buffer (Thermo Fisher Scientific) under gentle rotation for 10 minutes at room temperature

to lyse the majority of contaminating red blood cells. RBC lysis buffer was aspirated, and tumor pieces were washed with H+GPSA medium. Several tumor pieces were snap frozen for bulk RNA sequencing and whole exome sequencing. For histological studies, several tumor pieces were placed directly in 4% methanol-free formaldehyde (Polysciences) diluted in DPBS (Thermo Fisher Scientific) for 1 hour at room temperature under gentle rotation. After fixation, the tumor pieces were washed in DPBS and cryoprotected by overnight incubation in 30% sucrose (Sigma-Aldrich) in DPBS at 4°C. Tumor pieces were placed in a plastic cryomold (Electron Microscopy Sciences) and snap frozen in tissue freezing medium (General Data) on dry ice. Frozen tissue was stored at −80°C until processing.

Generation of GBOs from Resected Patient Glioblastoma Tissue—The remaining tumor pieces not set aside for RNA sequencing, whole exome sequencing, or histology were distributed in ultra-low attachment 6-well culture plates (Corning) with 4 mL of GBO medium containing 50% DMEM:F12 (Thermo Fisher Scientific), 50% Neurobasal (Thermo Fisher Scientific), 1X GlutaMax (Thermo Fisher Scientific), 1X NEAAs (Thermo Fisher Scientific), 1X PenStrep (Thermo Fisher Scientific), 1X N2 supplement (Thermo Fisher Scientific), 1XB27 w/o vitamin A supplement (Thermo Fisher Scientific), 1X 2-mercaptoethanol (Thermo Fisher Scientific), and 2.5 μg/ml human insulin (Sigma) per well and placed on an orbital shaker rotating at 120 rpm within a 37°C, 5% CO_2, and 90% humidity sterile incubator. Roughly 75% of the medium was changed every 48 hours by tilting the plates at a 45° angle and aspirating the medium above the sunken GBOs. Within the first week of culture, the tumor pieces often shed cellular and blood debris making the medium slightly cloudy. The shedding soon ceased, and the tumor pieces generally formed rounded organoids within 1-2 weeks, depending on tissue quality and patient-specific tumor growth characteristics. The criteria for successful establishment of GBOs from a given patient's tumor was that the micro-dissected tumor pieces survived for 2 weeks, developed a spherical morphology, and continuously grew in culture. GBOs cultured for prolonged periods of time (> 1 month) were routinely cut to ~200-500 μm diameter pieces using fine dissection scissors to prevent substantial necrosis within the center due to limited nutrient and oxygen diffusion. GBOs were sampled for RNA sequencing, whole exome sequencing, and histology by the same methods as the corresponding parental tumor pieces.

GBO Growth Analysis—To measure the growth of GBOs over time, similarly sized GBOs (0.5 −1 mm diameter) were placed into individual wells of a 48-well tissue culture plate with 300 μL of GBO medium per well. Images of individual GBOs were taken every week using a brightfield microscope and Zen software. The 2D projected area of each GBO was quantified in ImageJ by carefully outlining each GBO and measuring the area within the outlined region. The 2D area at each time point was divided by the 2D area at time 0 to calculate a growth ratio for each time point. Ten individual GBOs were measured for each GBO sample. GBOs recovered from the biobank were cultured for 3 days before the start of analysis of GBO growth.

Tissue Processing and Immunohistology—Serial tissue sections (20 μm for GBOs and 35 μm for xenografted rodent brains) were sliced using a cryostat (Leica, CM3050S), and melted onto charged slides (Thermo Fisher Scientific). Slides were dried at room

temperature and stored at −20°C until ready for immunohistology. For immunofluorescence staining, the tissue sections were outlined with a hydrophobic pen (Vector Laboratories) and washed with TBS containing 0.1% Tween-20 (v/v). Tissue sections were permeabilized and non-specific binding was blocked using a solution containing 10% donkey serum (v/v), 0.5% Triton X-100 (v/v), 1% BSA (w/v), 0.1% gelatin (w/v), and 22.52 mg/ml glycine in TBST for 1 hour at room temperature. For rodent brain sections, mouse-on-mouse blocking reagent (Vector Laboratories) was added to the blocking solution. The tissue sections were incubated with primary antibodies (see the Key Resources Table) diluted in TBST with 5% donkey serum (v/v) and 0.1% Triton X-100 (v/v) overnight at 4°C. After washing in TBST, the tissue sections were incubated with secondary antibodies (see the Key Resources Table) diluted in TBST with 5% donkey serum (v/v) and 0.1% Triton X-100 (v/v) for 1.5 hours at room temperature. After washing with TBST, sections were incubated with TrueBlack reagent (Biotium) diluted 1:20 in 70% ethanol for 1 minute to block autofluorescence due to lipofuscin and blood components. After washing with DPBS, slides were mounted in mounting solution (Vector Laboratories), coverslipped, and sealed with nail polish.

Tissue dehydration, paraffin embedding, microtome sectioning, and standard H&E staining was performed by the University of Pennsylvania Pathology Clinical Service Center. GBOs were fixed overnight in 4% methanol-free formaldehyde and stored in 70% ethanol at 4°C until ready for processing. GBOs and parental tumor samples were independently analyzed by an attending neuropathologist (M.N.).

Confocal Microscopy and Image Processing—Tumor tissue, GBOs, and brain sections were imaged as z stacks using a Zeiss LSM 810 confocal microscope or a Zeiss LSM 710 confocal microscope (Zeiss) using a 10X, 20X, 40X, or 63X objective with Zen 2 software (Zeiss). Images were analyzed using either Imaris 7.6 or ImageJ software. Images were cropped and edited using Adobe Photoshop (Adobe) and Adobe Illustrator (Adobe).

Detection of Hypoxia Gradients in GBOs—GBOs were incubated in GBO medium containing 200 μM pimonidazole-HCl (Hypoxyprobe) for three hours on an orbital shaker rotating at 120 rpm within a 37°C, 5% CO_2, 90% humidity sterile incubator and processed for immunohistology as described (Varia et al., 1998). Mouse anti-pimonidazole monoclonal antibody (Hypoxyprobe) was used to detect bound pimonidazole.

EdU Pulse-Chase in GBOs—GBOs were incubated in GBO medium containing 1 μM EdU (Thermo Fisher Scientific) for one hour on an orbital shaker rotating at 120 rpm within a 37°C, 5% CO_2, 90% humidity sterile incubator. GBOs were fixed and processed for immunohistology at 1-hourand 2-week time points. EdU incorporation was detected using Click-iT EdU Alexa Fluor 647 kit (Thermo Fisher Scientific) (Berg et al., 2019).

Biobanking and Recovery of GBOs—Within one month of culture, GBOs were cut into approximately 100 μm diameter pieces, washed with GBO medium to remove cell debris, and incubated with GBO medium supplemented with 10 μM Y-27632 (StemCell Technologies) for 1 hour. GBOs were resuspended in GBO freezing medium comprised of GBO medium supplemented with 10 μM Y-27632 and 10% DMSO (Sigma) and placed in cryovials (Thermo Fisher Scientific) with 20 GBOs per vial. GBOs were kept in the

cryovials with GBO freezing medium for 15 minutes at room temperature to allow the DMSO to better penetrate the core before slowly being cooled to −80°C using a CoolCell freezing container (Thermo Fisher Scientific) placed in a −80°C freezer. Frozen GBOs were placed in a liquid nitrogen tank for long-term storage. For recovery, vials were quickly thawed in a 37°C water bath, and GBOs were placed in a 50 mL conical tube. Ten ml of GBO medium containing 10 μM Y-27632 was added dropwise while vigorously swirling the tube to slowly dilute the DMSO. The medium was aspirated and GBOs were cultured overnight in GBO medium supplemented with 10 μM Y-27632. The medium was replaced with GBO medium without Y-27632 the next day. GBO pieces generally rounded up and were ready for experimentation within 1-2 weeks. All biobanked GBOs were confirmed free of Mycoplasma, Acholeplasma, and Spiroplasma with a detection limit of 10 CFU/ml by targeted PCR (Biological Industries).

Solid Tumor Sequencing Panel—The solid tumor sequencing panel was performed by the University of Pennsylvania Center for Personalized Diagnostics. Genomic DNA was extracted from fresh solid tumor specimens. Sequence analysis was performed on a panel of 152 genes: *ABL1, AKT1*, AKT2, AKT3*, ALK*, APC, AR*, ARAF*, ARID1A, ARID2, ATM, ATRX, AURKA, BAP1, BRAF*, BRCA1*, BRCA2, BRIP, BTK*, CREBBP*, CCND1, CCND2, CCND3, CCNE1,CDH1, CDK4, CDK6, CDKN2A, CHEK2*, CIC, CRKL, CSF1R, CTNNB1*, DAXX, DDR2*, DNMT3A, EIF1AX, EGFR*, EP300, EPHA3, ERBB2*, ERBB3, ERBB4, ERCC2, ERG, ESR1*, ESR2, EZH2, FBXW7, FGF3, FGFR1, FGFR2, FGFR3, FGFR4, FLT3, FUBP1, GATA3, GNA11*, GNAQ*, GNAS, HRAS*, H3F3A, IDH1*, IDH2*, IGF1R, JAK1, JAK2, JAK3, KDM5A, KDM5C, KDM6A, KDR*, KIT*, KMT2C, KRAS*, MAP2K1*, MAP2K2, MAP2K4, MAPK1, MAPK3, MAX, MCL1, MDM2, MDM4, MED12, MEN1, MET*, MITF, MLH1, MRE11A, MSH2, MSH6, MTOR, MYC, MYCN, NBN, NF1, NF2, NKRT1, NKRT2, NKRT3, NKX2-1, NOTCH1, NOTCH2, NOTCH3, NRAS*, PAK1, PALB2, PBRM1, PDGFRA*, PIK3CA*, PIK3CB, PIK3R1, PTCH1, PTEN, PTPN11, RAB35, RAC1, RAD50, RAD51, RAD51B, RAD51C, RAD51D, RAF1, RB1, RET*, RHOA, RNF43, SETD2, SF3B1, SLIT2, SMAD4, SMARCA4, SMO, SPOP, SRC, STAG2, STK11, SUFU, SUZ12, SYK, TET2, TGFBR2, TP53, TRAF7, TSC1, TSHR, TSC2, U2AF1, VHL, WT1*, and *XRCC2*. Targeted analysis for variants in the regions specified in this testing panel was achieved by enrichment of those genomic loci using a custom Agilent Haloplex assay. The library preparation included unique molecular identifiers to identify duplicate reads. Sequencing of enriched libraries was performed on the Illumina HiSeq 2500 platform using multiplexed, paired-end reads. Analyses and interpretation were performed using a customized bioinformatics pipeline, Halo_v1.2. All variants were annotated with reference to the hg19 Genome build. Variants were reported according to HGVS nomenclature and classified into 3 categories: disease-associated variants, variants of uncertain significance, and indeterminate. Variants internally classified as benign were not listed in the report. Variants determined to be clinically relevant but failing to meet technical reporting criteria were categorized as indeterminate. The lower limit of detection for single nucleotide variants (SNVs) and small insertions or deletions (indels) was established for this assay at 2% variable allele frequency. Categorization of variants was dependent upon multiple criteria, including (but not limited to) literature review and the presence of the variant in publicly available databases including

dbSNP, COSMIC, gnomAD, and the 1000 genome project. Copy number gain was inferred from this assay by increased read depth of the targeted regions which are designated above with an asterisk. Because analysis was conducted on a single piece of tissue, the results of this assay may not be representative of the entire tumor.

Fusion Transcript Panel—The fusion transcript panel was performed by the University of Pennsylvania Center for Personalized Diagnostics. RNA was extracted from formalin fixed paraffin embedded (FFPE) tumor tissue and reverse transcribed into cDNA allowing direct detection of normal and variant gene expression. PCR primers were designed to capture exons within transcripts of the following genes: *AKT1, ALK, AXL, BCOR, BRAF, CALCA, CAMTA1, CCNB3, CCND1, CIC, EGFR, EML4, EPC1, ERBB2, ERG, ESR1, EWSR1, FGFR1, FGFR2, FGFR3, FOXO1, FUS, GLI1, HMGA2, JAZF1, KRT20, KRT7, MEAF6, MET, MKL2, NCOA2, NRG1, NTRK1, NTRK2, NTRK3, PDGFB, PIK3CA, PLAG1, PMS2, PPARG, PTH, RAF1, RET, ROS1, SLC5A5, SS18, STAT6, TAF15, TCF12, TERT, TFE3, TFG, THADA, TMPRSS2, USP6*, and *YWHAE*. In addition, exons in internal housekeeping genes *CHMP2A, GPI, RAB7A*, and *VCP* were included as quality controls. The design of the panel was based on the literature at the time of development and the target regions were selected to include the most common fusion points of the specified genes. Sequencing of PCR-enriched libraries was performed on the Illumina HiSeq platform using multiplexed, paired-end reads. Analysis and interpretation utilized a customized bioinformatics pipeline, Archer_v6.0.3.2. All variants listed are with reference to the hg19 Genome build. The Archer Analysis 6.0.3.2 Software (ArcherDX, Inc.), was used to process the data and identify normal and abnormal reads. Because analysis was conducted on a single piece of tissue, the results of this assay may not be representative of the entire tumor.

MGMT Promoter Methylation Assay—The *MGMT* promoter methylation assay was performed by the University of Pennsylvania Center for Personalized Diagnostics. Genomic DNA was extracted from FFPE tumor tissue and underwent bisulfite conversion followed by amplification with primers to target *DMR2* of the *MGMT* (O-6-methylguanine-DNA methyltransferase) promoter, including 4 CpG sites (chr10:131,265,519-131,265,537; hg19 Assembly). Using pyrosequencing (PyroMark Q24, QIAGEN), the PCR product was evaluated to assess for percent methylation across the 4 CpG sites. The result was considered positive when the mean and median percent methylation across the 4 interrogated CpG sites was greater than or equal to 10%, considered low positive when the mean and median level of DNA methylation seen were either relatively low (above the limit of detection but below 10%) or highly variable across the CpG sites, and considered not detected when the mean and median percent methylation across the 4 CpG sites were below the limit of detection (4.5%). Appropriate positive and negative controls were included in each assay. Because analysis was conducted on a single piece of tissue, the results of this assay may not be representative of the entire tumor.

RNA Sequencing of Parental Tumors and Derived GBOs—In an effort to minimize variability due to sampling, we pooled 5-10 pieces of parental tumor tissue or GBOs into one sample for analyses. They were snap-frozen on dry ice, and stored at −80°C until processing. Samples were homogenized in TRIzol (Thermo Fisher Scientific) using a

disposable pestle and handheld motor. RNA clean-up was performed using a Zymo Research Clean & Concentrator kit after TRIzol (ThermoFisher) phase separation according to the manufacturers' protocol. RNA concentration and quality were assessed using a Nanodrop 2000 (Thermo Fisher Scientific).

Library preparation was performed as previously described with some minor modifications (Weng et al., 2017). About 100 ng RNA in 3.2 μL was combined with 0.25 μL RNase inhibitor (NEB) and 1 μL CDS primer (5′-AAGCAGTGGTATCAACGCAGAGTACT30VN-3′) in an 8-well PCR tube strip, heated to 70°C, and immediately placed on ice. 5.55 μL RT mix, containing 2 μL of 5X SMARTScribe RT buffer (Takara), 0.5 μL of 100 mM DTT (Millipore Sigma), 0.3 μL of 200 mM $MgCl_2$ (Thermo Fisher Scientific), 1 μL of 10 mM dNTPs (Takara), 1 μL of 10 μM TSO primer (5′-AAGCAGTGGTATCAACGCAGAGTACATrGrGrG-3′), 0.25 μL of RNase inhibitor (NEB), and 0.5 μL SMARTScribe reverse transcriptase (Takara) was added to the reaction. RT was performed under the following conditions: 42°C for 90 minutes, 10 cycles of 50°C for 2 minutes and 42°C for 2 minutes, 70°C for 15 minutes, and 4°C indefinitely. For cDNA amplification, 2 μL of the RT reaction was combined with 2.5 μL of 10X Advantage 2 buffer (Takara), 0.5 μL of 10 mM dNTPs (Takara), 0.25 μL of 10 mM IS PCR primer (5′-AAGCAGTGGTATCAACGCAGAGT-3′), 19.25 μL nuclease free water (ThermoFisher), and 0.5 μL Advantage 2 DNA Polymerase (Takara). Thermocycling conditions were as follows: 94°C for 3 minutes, 8 cycles of 94°C for 15 s, 65°C for 30 s, and 68°C for 6 minutes, 72°C for 10 minutes, and 4°C indefinitely. Amplified cDNA was purified using 0.8X SPRI beads (Beckman Coulter), eluted in 10 μL nuclease-free water, and quantified using Qubit dsDNA HS assay kit (Thermo Fisher Scientific). cDNA was fragmented by combining 100 pg cDNA in 1 μL with 1 μL nuclease free water, 2X TD buffer (20 mM Tris, pH 8.0 (Thermo Fisher Scientific), 10 mM MgCl2, and 16% PEG 8000 (MilliporeSigma), and 0.5 μL Tn5 (Lucigen). The mixture was heated to 55°C for 10 minutes, and the reaction was terminated upon the addition of 1.25 μL of 0.2% SDS (Fisher) and incubation at room temperature for 10 minutes. Fragments were amplified by adding 27.75 μL nuclease free water (Thermo Fisher Scientific), 10 μL of 5X KAPA HiFi Fidelity Buffer (Roche), 10 mM dNTPs (Roche), 1 μL of 10 mM Nextera i7 primer, 1 μL of 10 mM Nextera i5 primer, and 2 μL KAPA HiFi Polymerase (Roche). Thermocycling conditions were as follows: 72°C for 5 minutes, 95°C for 1 minute, 14 cycles of 95°C for 30 s, 55°C for 30 s, and 72°C for 30 s, 72°C for 1 minute, and 4°C indefinitely. DNA was purified twice with 0.8X SPRI beads (Beckman Coulter) and eluted in 10 μL of 10 mM Tris, pH 8 (Thermo Fisher Scientific). Samples were quantified by qPCR (KAPA) and pooled at equal molar amounts. Final sequencing library fragment sizes were quantified by bioanalyzer (Agilent) with an average size of ~350 bp, and concentrations were determined by qPCR (KAPA). Samples were loaded at concentrations of 2.2 pM, and sequenced on a NextSeq 550 (Illumina) using 2x76 bp reads to an average depth of 25 million reads per sample.

Raw sequencing data were demultiplexed with bcl2fastq2 v.2.19.0.316 (Illumina) with adaptor trimming turned off. Alignment was performed using STAR v.2.6.1d (Dobin et al., 2013) with the following additional parameters: *–outFilterMatchNminOverLread 0.33–outFilterScoreMinOverLread 0.33–twopassMode Basic–chimSegmentMin 12–chimJunctionOverhangMin 12–alignSJDBoverhangMin 1–alignMatesGapMax 100000–*

alignIntronMax 200000–chimSegmentReadGapMax 3–alignSJstitchMismatchNmax 5 –1 5 5–outSAMstrandField intronMotif–chimOutJunctionFormat 1. GRCh38 (gencode) was used as the reference genome, and gencode v.28 GTF was used as the annotation file. Multimapping and chimeric alignments were discarded, and uniquely mapped reads were quantified at the exon level and summarized to gene counts using Rsubread (Liao et al., 2019). Counts were converted to units of TPM, and batch correction was performed using SVA (Leek et al., 2012). Further analyses were performed in R v.3.5.1.

Pearson's correlation coefficient was calculated across all genes that were detected in at least one sample in the final dataset. To identify highly variable genes in the primary tumors, the coefficient of variation of the expression of each gene was modeled against the mean expression in $\log_{10}$ scale using a LOESS regression. The top 10,000 genes with the greatest positive deviation from the fit and a mean expression of greater than 1 TPM were selected.

Differential gene expression analysis (Figures S3D–S3F) was performed using the DESeq2 suite of analysis tools (Love et al., 2014). Time course analysis was performed using the likelihood ratio test where the full model design was *~Batch + Tumor + Time point* and the reduced model design was *~Batch + Tumor*. Cutoffs for significance were set at Benjamini-Hochberg corrected p value < 0.01 and $\log_2$ fold change > 2. Gene ontology enrichment analysis was performed using Enrichr (Kuleshov et al., 2016). Regional sample PCA analysis was also performed using the DESeq2 suite of tools, including VST transformation of raw counts and selection of the top 100 most variably expressed genes for PCA analysis.

EGFRvIII transcripts were detected by RNA-seq and quantified by examining the number of exon 1 to exon 8 spanning reads versus the number of exon 7 to exon 8 spanning reads (Brennan et al., 2013). 95% credible intervals were determined using a beta distribution with a uniform prior.

Whole Exome Sequencing of Parental Tumors and Derived GBOs—At least 5-10 pieces of parent tumor or GBOs at 2 weeks were combined into one sample, snap-frozen on dry ice, and stored at −80°C until processing. A 50 μL aliquot of whole blood obtained at the time of surgery was also snap-frozen on dry ice and stored at −80°C until processing. DNA was extracted using the Zymo *Quick*-DNA Microprep Kit. DNA quality were assessed using a Nanodrop 2000 (Thermo Fisher Scientific) and quantified using the Qubit high sensitivity dsDNA assay (Thermo Fisher Scientific). Exomeseq libraries were prepared using the Nextera Flex for Enrichment kit (Illumina), Illumina exome panel oligos (Illumina), and IDT for Illumina DNA UD set A index primers (Illumina) according to the manufacturer's instructions. Genomic DNA inputs varied from 25 to 300 μg, and pre-enrichment samples were combined at equal amounts by mass in 9 or 10 plex pools for enrichment. Sequencing library fragment sizes were quantified by bioanalyzer (Agilent), and concentrations were quantified by qPCR (KAPA). Samples were combined into 18- or 19-plex equimolar pools with whole blood, corresponding parental tumor, and corresponding GBO combined in the same sequencing run, loaded at a concentration of 2.2 pM, and sequenced on a NextSeq 550 (Illumina) using 2x74 bp reads for an average of 32 million reads per sample and an average target coverage of 47x.

Raw sequencing data were demultiplexed with bcl2fastq2 with adaptor trimming turned off. Alignment was performed using BWA-MEM with default parameters and a GRCh38 reference genome kindly provided by the Broad Institute on a public GATK resource FTP server (Li and Durbin, 2009). Pre-processing according to GATK best practices, including marking PCR duplicates and base quality recalibration, was performed using Picard tools v.1.141 and GATK v.4.1.0.0. (DePristo et al., 2011; McKenna et al., 2010; Van der Auwera et al., 2013). A database of known polymorphic sites was used from the GATK resource bundle based on dbSNP build 146.

Somatic variants were identified using four different variant calling tools: Mutect2, Varscan2, Freebayes, and Manta/Strelka2. Mutect2 was run with a panel of normals composed of the 11 samples used in this study, a population germline variant resource from gnomAD (Broad Institute), and allele frequencies of variants not included in the germline resource set to 0.0000025 (Cibulskis et al., 2013). GATK contamination detection was performed using a small ExAC reference provided by the GATK resource bundle, and filtering was performed using default parameters. Varscan2 was run using default parameters, and somatic variants were filtered for a p value < 0.05 and alternate allele frequency > 0.05 (Koboldt et al., 2012; Li et al., 2009). Freebayes was run in somatic mode with the following additional parameters (Garrison and Math, 2012): *-F 0.05–pooled-continuous–pooled-discrete*. Variants were filtered using vcflib by breaking multiallelic records into separate lines, identifying putative somatic variants by comparison with the paired whole blood sample, filtering for variant calls where the QUAL field > 20, and filtering for variant calls where the coverage was > 20. Prior to running Strelka2, Manta was used to call candidate somatic indels in exome mode across only the primary GRCh38 contigs (Chen et al., 2016). Then, Strelka2 was run in exome mode using identified candidate indels also across the primary GRCh38 contigs to identify somatic variants (Kim et al., 2018). Somatic variants were filtered using default settings. VCFtools was used for variant manipulations throughout these analyses (Danecek et al., 2011).

Identified somatic variants in the individual samples were called if identified by two or more variant calling tools using the above described workflow. Variants identified in the parental tumor and corresponding GBOs were pooled to yield a final variant list. Allele frequencies were queried at these sites in the parental tumors and corresponding GBOs using bcftools mpileup accepting anomalous read pairs and disabling probabilistic realignment for base alignment quality calculation (Li, 2011). This approach of “recovering” variants is inspired by previous work in cancer organoids (Kopper et al., 2019). Annovar was used to annotate variants with the following databases (Wang et al., 2010): RefGene (2017), dbNSFP35a (Liu et al., 2011, 2016), COSMIC v88 (Forbes et al., 2017), Clin-Var (Landrum et al., 2016), and avsnp (based on dbsnp 150). Variants highlighted in Figure 3C come from a list of significantly mutated genes from work by Brennan et al. (2013).

Copy number analysis was performed using the GATK4 pipeline. A target manifest was obtained from the exome panel supplier (Illumina) in hg19 coordinates and lifted over to GRCh38 coordinates using Picard tools and a chain file from UCSC genome browser. Allosomal chromosomes were excluded and all whole blood samples were included in the construction of a panel of normals. Read counts were quantified and denoised using GATK.

Allele counts were quantified over a set of genomic intervals defined by a subset of gnomad snps provided in the GATK resource bundle. Genomic segments were modeled with the following additional parameters: *–number-of-smoothing-iterations-per-fit 1–number-of-changepoints-penalty-factor 5*. Copy ratios were called and visualized using IGV (Robinson et al., 2011). Copy ratios with a greater than 10% change and with the most number of independent probes supporting the call were summarized to chromosomal arms and shown in Figure 3C.

Tissue Dissociation and Single-cell RNA Sequencing—Multiple tumor pieces and GBOs were dissociated using a papain-based neural tissue dissociation kit (Miltenyi Biotech). Crude dissociates from parental tumor samples were treated with ammonium chloride based RBC lysis buffer (Thermo Fisher Scientific) for 5 minutes. All samples were washed three times by centrifugation at 200 g for 5 minutes and resuspension in 10 mL of calcium-free, magnesium-free DPBS (Thermo Fisher Scientific). Cells were strained through a 70 μm filter (Miltenyi Biotech), analyzed for viability by trypan blue staining, and counted using an automatic cell counter (Thermo Fisher Scientific). Samples had a viability of >80% and were diluted to a final concentration of 100 viable cells/μL in DPBS with 0.01% BSA(w/v). Single cell droplet encapsulation and library preparation was performed using the drop-seq method with minor modifications (Macosko et al., 2015). Microfluidic chips were obtained from FlowJEM with plasma bonding and aquapel treatment using the same design as previously published. Each droplet co-encapsulation run was performed with 50% additional reagent volume to account for syringe and tubing dead volume as well as occasional microfluidic channel clogging and re-starts. Each sample was loaded onto 2-4 droplet generation runs, and cell suspensions and droplets were kept on ice prior to droplet encapsulation and droplet breakage. In the cDNA PCR amplification stage, between 4,000-8,000 beads were combined in a single PCR tube reaction and purified individually using 0.6x SPRI beads (Beckman Coulter). cDNA across multiple runs of the same sample were pooled together and used as input for tagmentation, where the tagment reaction time was increased to 8 minutes. Final samples were purified once with 0.6x SPRI beads and a second time with 1.0x SPRI beads (Beckman Coulter). Sequencing library fragment sizes were quantified by bioanalyzer (Agilent), and concentrations were quantified by qPCR (KAPA). Samples were pooled, loaded at 2.2 pM, and sequenced on a NextSeq 550 (Illumina) with a 20 bp Read 1 and 64 bp Read 2. The custom Read 1 primer was spiked into the usual Illumina sequencing primer well (#20) at the manufacturer's recommended concentration.

Raw sequencing data was demultiplexed with bcl2fastq2 (Illumina) with adaptor trimming turned off. Additional processing was performed using drop-seq tools v.2.1.0 with GRCh38 as the reference genome, and gencode v.28 GTF was used as the annotation file (Saunders et al., 2018). Seurat v3.1 was used to analyze the scRNA-seq data (Stuart et al., 2019). Cells with > 400 unique genes detected, < 5,000 genes detected, and < 25% mitochondrial reads were retained for further analysis. Standard pre-processing pipelines, including normalization and scaling, were followed without additional modifications. Clustering and UMAP dimensionality reduction were performed based on empirically selected PCs.

For CNA analysis, inferCNV was used (Patel et al., 2014; Tirosh et al., 2016; Venteicher et al., 2017) on each patient sample individually with microglia/macrophages and T cells set as references (Figure S4A). Non-neoplastic cells were identified by the expression of classical markers. Microglia/macrophages were further sub-setted for detailed analysis. Expression of genes associated with microglia or macrophages (Darmanis et al., 2017) was calculated using the AddModuleScore function in Seurat with bin size set to 10. Enrichment of macrophage versus microglia gene expression was taken as the difference between the gene signature expressions.

To compare the parental tumor and derived GBOs at 2 weeks, gene expression within clusters were averaged and compared by calculating the transcriptome-wide Pearson correlation. Hierarchical clustering was performed using Euclidian distances of correlations to the primary tumor. Cluster specific marker expression was determined using the Wilcoxon rank sum test. For comparison with normal brain cell types, two single-nuclei RNA-seq datasets of normal adult human cerebral cortex were retrieved from public repositories (Habib et al., 2017; Lake et al., 2018). These datasets were selected because they were generated using adaptations of the drop-seq platform and were expected to best match the technical characteristics of our single-cell RNA-seq data. Annotated granule, CA1, and CA3 neurons were excluded, and all other neuron types were combined as one large neuronal population in the downstream analysis. Differential gene expression was performed using the FindAllMarkers function in Seurat with a log fold-change threshold of 0.1 and a minimum percent expressed threshold of 0.1. The top 100 marker genes based on adjusted p value were selected for each cell type. Gene enrichment was calculated from these marker gene lists in the GBO single-cell RNA-seq data using the AddModuleScore function with the number of bins set to 10 and averaged across all cells in each GBO cluster.

Digital PCR for EGFR and EGFRvIII Transcripts—Primers and minor groove binder (MGB) probes for WT *EGFR* and *EGFRvIII* were designed. The WT *EGFR* MGB probe was fluorescently labeled with 6-FAM and the *EGFRvIII* MGB probe was fluorescently labeled with 6-FAM or VIC. Gene copies per µl were normalized with the VIC labeled internal reference control RNase P (Thermo Fisher Scientific) by running a parallel reaction on the same chip with either FAM labeled WT *EGFR* or *EGFRvIII* reaction mix. The Digital PCR reactions were carried out using Quantstudio 3D digital PCR master mix V2 (Applied Biosystems) following the manufacturer's instructions. The chips were loaded onto a Thermal cycler (ProFlex PCR system, Applied Biosystems) and each individual chip was read on a chip reader (Quantstudio 3D Digital PCR Instrument, Applied Biosystems). For each chip, the instrument generated a single.eds file that contained the processed imaged data and the results from preliminary analysis on the instrument. The data were then transferred onto the Thermo Fisher Scientific cloud for further analysis by the software. Tumor samples and GBOs were analyzed for WT *EGFR* and *EGFRvIII*. For every tumor and GBO sample, two chips were run separately with the same concentration of cDNA containing *EGFRvIII* primers with *RNaseP* (VIC labeled) and probe for WT *EGFR* (FAM labeled), respectively. WT *EGFR* and *EGFRvIII* copies per µl were normalized with *RNaseP* (internal control). Amplified *EGFR* was considered positive if the ratio of WT *EGFR* to *RNaseP* was ≥ 1.5. *EGFRvIII* is considered positive if *vIII* % is ≥ 10%.

Animals and Orthotopic Transplantation of GBOs—Orthotopic transplantation of GBOs was performed using a method described for brain organoid transplantation into immunodeficient mice (Mansour et al., 2018). Mice were induced into anesthesia with 5% and maintained with 2% isoflurane in oxygen. An approximately 1 mm^2 craniotomy above the right cerebral cortex at the intersection between the sagittal and lambdoid sutures was performed using a micromotor drill (Stoelting). After removing the meninges, the underlying brain tissue was aspirated using a 23G blunt needle (Neta Scientific) to create a 1 mm^3 cavity. Bleeding was controlled using Gelfoam (Pfizer) and sterile saline. A single GBO was transferred into the cavity and sealed by 3-mm coverslipand super glue (Bob Smith Industries), followed by application of dental cement (Benco Dental) onto the surrounding skull area. Each transplanted GBO was approximately 1 mm in diameter and consisted of roughly 1 million cells as determined by automated cell counting (Countess II, Thermo Fisher Scientific) of similarly sized GBOs. Animals were weighed twice a week and euthanized immediately after weight loss and/or the onset of neurological symptoms. Anesthesia by intraperitoneal injection of a lethal dose of ketamine, xylazine and acepromazine cocktail was performed. Mice were transcardially perfused with cold 0.1 M phosphate buffer followed by cold 4% formaldehyde in 0.1 M phosphate buffer (pH 7.4). Brains were carefully removed from the skull and fixed in 4% formaldehyde at 4°C overnight, washed with DPBS, and cryoprotected in 30% sucrose (w/v) overnight at 4°C. Brains were placed in plastic cryomolds and snap frozen in tissue freezing medium (General Data) on dry ice. Frozen brains were stored at −80°C until processing.

Radiation and Drug Treatment of GBOs—For radiation experiments, GBOs were irradiated at a total dose of 10 Gray (Gy) at a dose rate of 2.65 Gy/min using a Precision XRAD320iX cabinet irradiator with 320 kV voltage, 12.5 mA current, and 50 source to surface distance (SSD). For drug experiments, GBOs were cultured for a week in GBO medium containing either 50 μM temozolomide (Santa Cruz Biotechnology), 5 μM gefitinib (Santa Cruz Biotechnology), 1 μM trametinib (Santa Cruz Biotechnology), 1 μM everolimus (Santa Cruz Biotechnology), or DMSO vehicle on an orbital shaker rotating at 120 rpm within a 37°C, 5% CO_2, and 90% humidity sterile incubator. Media containing fresh drug was replaced every 48 hours. Different batches of GBOs were used for different treatment experiments (See Table S6 for their ages in culture). For a given treatment, GBOs were treated in triplicate and quantified for DAPI and KI67 immunohistology. Samples were subsequently stratified based on a statistically significant reduction in the percentage of $KI67^+$ nuclei for gene expression analyses. Gene Set Enrichment Analysis (Subramanian et al., 2005), based on normalized expression value (TPM) from RNA-seq of pretreatment GBOs and parental tumors, was performed using GenePattern from the publicly available Broad Institute Servers (cloud.genepattern.org).

GBO size experiments were performed utilizing biobanked samples that were recovered for a minimum of 2 weeks prior to use. GBOs of similar size were placed in individual wells of a 24-well plate in 1 mL of GBO media containing drug or vehicle control. Similar to GBO growth analyses, images of individual GBOs were taken on a weekly basis using a brightfield microscope and Zen software. The 2D projected area of each GBO was quantified in ImageJ by manually outlining each GBO and measuring the area within the

outlined region. GBO size was calculated as the ratio of the measured 2D projected area at each time point to the measured 2D area at time point 0. Analysis was done in the form of growth over time following 1 week of drug exposure of 1 μM trametinib (Santa Cruz Biotechnology), or 1 μM everolimus (Santa Cruz Biotechnology) and subsequent growth for 2 additional weeks in normal GBO media. GBO growth was also analyzed in the form of dose response with serial dilutions of trametinib and everolimus ranging from 0.1 nM to 1000 nM with GBO size measurement after 1 week of drug exposure.

For *in vivo* drug treatment experiments, UP-7790-GBOs were recovered from the biobank and cultured *in vitro* for 14 days before xenografting individual organoids into female adult athymic nude (NU/J) mice. At 14 days after xenograft, mice were randomized into treatment groups and given daily intraperitoneal injections of either vehicle (10% DMSO, 90% corn oil) or trametinib (3 mg/kg) for 12 days. Mice were weighed every other day to monitor animal health. Mice were given a single injection of EdU (10 mg/kg) 2 hours before sacrificing. Xenografts were analyzed using immunohistology for proliferation (KI67 and EdU) and cell death (Cleaved-Caspase-3). Quantifications were performed blind to the treatment groups.

Generation of CD19 and 2173BBz CAR-T Cells and GBO-CAR-T Co-culture—T cells were isolated from leukapheresis products obtained from de-identified healthy donors under a protocol approved by the University of Pennsylvania's Institutional Review Board. T cells were stimulated with Dynabeads Human T-Activator CD3/CD28 (Thermo Fisher Scientific) at a bead to cell ratio of 3:1 (first stimulation) and transduced with lentiviral vector coding CAR transgene. T cells were cultured in RPMI 1640 medium supplemented with 10% fetal bovine serum, 20 mM HEPES, and PenStrep (Thermo Fisher Scientific) and medium was replaced every 48 hours. The end of the first stimulation was determined by decreased log-phase growth and reduced mean lymphocytic volume to 300-330 fl as measured on a Coulter Multisizer. This was usually reached 10 days after stimulation, and the T cells were frozen down for functional assays or used for re-stimulation. The percentage of T cells expressing CARs was determined by flow cytometry (LSR II, BD Biosciences) using biotinylated anti-human and anti-mouse antibodies for 2173BBz and CD19 CAR-T cells, respectively, with streptavidin-coupled PE. Data were analyzed using FlowJo software. In the current study, T cells transduced with CD19 and 2173BBz CARs were 30% and 32% CAR^+, respectively.

Vials containing frozen CD19 and 2173BBz CAR-T cells were recovered in ImmunoCult-XF T Cell Expansion Medium (StemCell Technologies) with 100 units/ml of recombinant human IL-2 (StemCell Technologies). After 24 hours, the medium was replaced with ImmunoCult-XF T Cell Expansion Medium without IL-2 and the T cells were cultured for an additional 48 hours. T cells were incubated with GBOs in ultra-low attachment 24-well culture plates (Corning) at a ratio of approximately one T cell for every ten GBO cells (30,000 T cells and a single organoid in one well) with 1 mL of ImmunoCult-XF T Cell Expansion Medium per well. Cell counts within GBOs were estimated by dissociating similarly sized GBOs from each patient followed by automated cell counting (Countess II, Thermo Fisher Scientific Scientific). The plates were placed on an orbital shaker rotating at 120 rpm within a 37°C, 5% CO_2, 90% humidity sterile incubator. Co-culture experiments

were performed for six GBO samples with triplicates for each condition. The GBO-CAR-T co-cultures were monitored by brightfield microscopy at 0,1,2, and 3 day time points with samples taken for immunohistological analysis at 0, 1 and 3 days.

Cytokine ELISA—For each experimental condition, 200 μL of medium was sampled at 0,1, and 3-day time points after GBO-CAR-T co-culture from the same well, snap frozen on dry ice, and stored at −80°C until ready for analysis. Displaced medium was replaced with 200 μL of ImmunoCult-XF T Cell Expansion Medium to prevent concentration of cytokines. An ELISA was performed in triplicates on 10-fold diluted medium using human IL-2, IFN-γ, and TNF-α DuoSet ELISA kits (R&D) and absorbances were recorded at 450 nm using a microplate absorbance reader (BioRad). The absorbance value at 450 nm for the blank condition was subtracted from the experimental values. Seven-point standard curves were used to calculate cytokine concentrations from absorbance values.

QUANTIFICATION AND STATISTICAL ANALYSIS

Studies were not blinded with the exception for analysis of *in vivo* drug treatments. All statistical tests and sample sizes are included in the Figure Legends and text. All data are shown as mean ± SEM. In all cases, the p values are represented as follows: ***$p < 0.001$, ** $p < 0.01$, *$p < 0.05$, and not statistically significant when $p > 0.05$. In all cases, the stated "n" value is either parental tumor pieces, GBOs, or mice with multiple independent images used to obtain data points for each. No statistical methods were used to pre-determine sample sizes. For all quantifications of immunohistology, the samples being compared were processed in parallel and imaged using the same settings and laser power for confocal microscopy. Immuno-positive cells were quantified manually using the cell counter function in ImageJ (NIH). Images from the outer region of five organoids were used for quantification and compared to healthy, non-necrotic regions from five different pieces of the parental tumors. Fluorescence intensity was quantified by outlining the region of interest and using the measure function in ImageJ (NIH) to obtain the mean gray value for the marker of interest. To quantify the number of migrated tumor cells, we created "spots" for each individual cell based on immunofluorescent staining for human nuclear antigen, then drew "surfaces" by outlining the contour of the coronal brain section as well as initial graft site in Imaris (Bitplane) based on aligned image stacks as previously described (Sun et al., 2015). For 3-D reconstruction, optical stacks of images were serially aligned along the rostro-caudal axis using Reconstruct 1.1.0 (J.C. Fiala, NIH). The extent of infiltration was quantified using STEM121 immunofluorescence. Concentric rings were drawn using ImageJ to measure the distance of the furthest infiltrated cells from the margin of the initial graft site, and the scores were assigned as 0 (no infiltration), 1 (< 2 mm), 2 (2-4 mm) and 3 (> 4 mm). All quantifications of cell counts were statistically analyzed using a Student's t test performed using GraphPad Prism (GraphPad Software Inc). Statistical analysis of CD3, Cleaved-caspase-3, and EGFRvIII/EGFR fluorescent intensities and cytokine concentrations by ELISAs was performed using two-way-ANOVA with uncorrected Fisher's LSD test using GraphPad Prism.

DATA AND CODE AVAILABILITY

The access number for the RNA-seq, exome-seq and single-cell RNA-seq data reported in this study is NCBI GEO: GSE141947.

Supplementary Material

Refer to Web version on PubMed Central for supplementary material.

ACKNOWLEDGMENTS

We would like to thank all patients who generously donated tissue. We thank members of the Ming and Song laboratories, the Glioblastoma Translational Center of Excellence, and D. Lim for comments and suggestions; A.A. Mansour and F.H. Gage for initial guidance of the transplantation procedure; B. Temsamrit and E. LaNoce for technical support; W. Sarchiapone for assistance with clinical information; and K. Abdullah, E. Hudgins, and M. Piazza for assistance with tissue acquisition. The graphical abstract was created using illustrations from https://www.biorender.com. This work was partially supported by Glioblastoma Translational Center of Excellence at the Abramson Cancer Center, NIH (R37NS047344 to H.S. and R35NS097370 and U19AI131130 to G.-l.M.), and the Sheldon G.Adelson Medical Research Foundation (to G.-l.M.). D.Y.Z. was partially supported by the Blavatnik Family Fellowship in Biomedical Research. P.T.T.N. was partially supported by the Hearst Foundation Fellowship.

REFERENCES

Arif SH, Pandith AA, Tabasum R, Ramzan AU, Singh S, Siddiqi MA, and Bhat AR (2018). Significant Effect of Anti-tyrosine Kinase Inhibitor (Gefitinib) on Overall Survival of the Glioblastoma Multiforme Patients in the Backdrop of Mutational Status of Epidermal Growth Factor Receptor and *PTEN* Genes. Asian J. Neurosurg 13, 46–52. [PubMed: 29492119]

Backos DS, Franklin CC, and Reigan P (2012). The role of glutathione in brain tumor drug resistance. Biochem. Pharmacol 83, 1005–1012. [PubMed: 22138445]

Bagley SJ, Schwab RD, Nelson E,Viaene AN, Binder ZA, Lustig RA, O'Rourke DM, Brem S, Desai AS, and Nasrallah MP (2019). Histopathologic quantification of viable tumor versus treatment effect in surgically resected recurrent glioblastoma. J. Neurooncol 141, 421–429. [PubMed: 30446903]

Berg DA, Su Y, Jimenez-Cyrus D, Patel A, Huang N, Morizet D, Lee S, Shah R, Ringeling FR, Jain R, et al. (2019). A Common Embryonic Origin of Stem Cells Drives Developmental and Adult Neurogenesis. Cell 177, 654–668. [PubMed: 30929900]

Bian S, Repic M, Guo Z, Kavirayani A, Burkard T, Bagley JA, Krauditsch C, and Knoblich JA (2018). Genetically engineered cerebral organoids model brain tumor formation. Nat. Methods 15, 631–639. [PubMed: 30038414]

Bigner SH, Humphrey PA, Wong AJ, Vogelstein B, Mark J, Friedman HS, and Bigner DD (1990). Characterization of the epidermal growth factor receptor in human glioma cell lines and xenografts. Cancer Res. 50, 8017–8022. [PubMed: 2253244]

Bleijs M, van de Wetering M, Clevers H, and Drost J (2019). Xenograft and organoid model systems in cancer research. EMBO J. 38, e101654. [PubMed: 31282586]

Boj SF, Hwang CI, Baker LA, Chio II, Engle DD, Corbo V, Jager M, Ponz-Sarvise M, Tiriac H, Spector MS, et al. (2015). Organoid models of human and mouse ductal pancreatic cancer. Cell 160, 324–338. [PubMed: 25557080]

Brandes AA, Franceschi E, Tosoni A, Blatt V, Pession A, Tallini G, Bertorelle R, Bartolini S, Calbucci F, Andreoli A, et al. (2008). MGMT promoter methylation status can predict the incidence and outcome of pseudoprogression after concomitant radiochemotherapy in newly diagnosed glioblastoma patients. J. Clin. Oncol 26, 2192–2197. [PubMed: 18445844]

Brennan CW, Verhaak RG, McKenna A, Campos B, Noushmehr H, Salama SR, Zheng S, Chakravarty D, Sanborn JZ, Berman SH, et al. TCGA Research Network (2013). The somatic genomic landscape of glioblastoma. Cell 155, 462–477. [PubMed: 24120142]

Broutier L, Mastrogiovanni G, Verstegen MM, Francies HE, Gavarró LM, Bradshaw CR, Allen GE, Arnes-Benito R, Sidorova O, Gaspersz MP, et al. (2017). Human primary liver cancer-derived organoid cultures for disease modeling and drug screening. Nat. Med 23, 1424–1435. [PubMed: 29131160]

Chen X, Schulz-Trieglaff O, Shaw R, Barnes B, Schlesinger F, Källberg M, Cox AJ, Kruglyak S, and Saunders CT (2016). Manta: rapid detection of structural variants and indels for germline and cancer sequencing applications. Bioinformatics 32, 1220–1222. [PubMed: 26647377]

Cibulskis K, Lawrence MS, Carter SL, Sivachenko A, Jaffe D, Sougnez C, Gabriel S, Meyerson M, Lander ES, and Getz G (2013). Sensitive detection of somatic point mutations in impure and heterogeneous cancer samples. Nat. Biotechnol 31, 213–219. [PubMed: 23396013]

Clevers H (2016). Modeling Development and Disease with Organoids. Cell 165, 1586–1597. [PubMed: 27315476]

da Silva B, Mathew RK, Polson ES, Williams J, and Wurdak H (2018). Spontaneous Glioblastoma Spheroid Infiltration of Early-Stage Cerebral Organoids Models Brain Tumor Invasion. SLAS Discov. 23, 862–868. [PubMed: 29543559]

Danecek P, Auton A, Abecasis G, Albers CA, Banks E, DePristo MA, Handsaker RE, Lunter G, Marth GT, Sherry ST, et al. 1000 Genomes Project Analysis Group (2011). The variant call format and VCFtools. Bioinformatics 27, 2156–2158. [PubMed: 21653522]

Darmanis S, Sloan SA, Croote D, Mignardi M, Chernikova S, Samghababi P, Zhang Y, Neff N, Kowarsky M, Caneda C, et al. (2017). Single-Cell RNA-Seq Analysis of Infiltrating Neoplastic Cells at the Migrating Front of Human Glioblastoma. Cell Rep. 21, 1399–1410. [PubMed: 29091775]

de Bruin EC, Cowell C, Warne PH, Jiang M, Saunders RE, Melnick MA, Gettinger S, Walther Z, Wurtz A, Heynen GJ, et al. (2014). Reduced NF1 expression confers resistance to EGFR inhibition in lung cancer. Cancer Discov. 4, 606–619. [PubMed: 24535670]

DePristo MA, Banks E, Poplin R, Garimella KV, Maguire JR, Hartl C, Philippakis AA, del Angel G, Rivas MA, Hanna M, et al. (2011). A framework for variation discovery and genotyping using next-generation DNA sequencing data. Nat. Genet 43, 491–498. [PubMed: 21478889]

Dobin A, Davis CA, Schlesinger F, Drenkow J, Zaleski C, Jha S, Batut P, Chaisson M, and Gingeras TR (2013). STAR: ultrafast universal RNA-seq aligner. Bioinformatics 20, 15–21.

Forbes SA, Beare D, Boutselakis H, Bamford S, Bindal N, Tate J, Cole CG, Ward S, Dawson E, Ponting L, et al. (2017). COSMIC: somatic cancer genetics at high-resolution. Nucleic Acids Res. 45 (D1), D777–D783. [PubMed: 27899578]

Gao D, Vela I, Sboner A, Iaquinta PJ, Karthaus WR, Gopalan A, Dowling C, Wanjala JN, Undvall EA, Arora VK, et al. (2014). Organoid cultures derived from patients with advanced prostate cancer. Cell 159, 176–187. [PubMed: 25201530]

Garrison E, and Math G (2012). Haplotype-based variant detection from short-read sequencing. arXiv, arXiv:1207.3907.

Giannini C, Sarkaria JN, Saito A, Uhm JH, Galanis E, Carlson BL, Schroeder MA, and James CD (2005). Patient tumor EGFR and PDGFRA gene amplifications retained in an invasive intracranial xenograft model of glioblastoma multiforme. Neuro-oncol. 7, 164–176. [PubMed: 15831234]

Gjorevski N, Sachs N, Manfrin A, Giger S, Bragina ME, Ordóñez-Morán P, Clevers H, and Lutolf MP (2016). Designer matrices for intestinal stem cell and organoid culture. Nature 539, 560–564. [PubMed: 27851739]

Goff SL, Morgan RA, Yang JC, Sherry RM, Robbins PF, Restifo NP, Feldman SA, Lu YC, Lu L, Zheng Z, et al. (2019). Pilot Trial of Adoptive Transfer of Chimeric Antigen Receptor-transduced T Cells Targeting EGFRvIII in Patients With Glioblastoma. J. Immunother 42, 126–135. [PubMed: 30882547]

Habib N, Avraham-Davidi I, Basu A, Burks T, Shekhar K, Hofree M, Choudhury SR, Aguet F, Gelfand E, Ardlie K, et al. (2017). Massively parallel single-nucleus RNA-seq with DroNc-seq. Nat. Methods 14, 955–958. [PubMed: 28846088]

Huang L, and Fu L (2015). Mechanisms of resistance to EGFR tyrosine kinase inhibitors. Acta Pharm. Sin. B 5, 390–401. [PubMed: 26579470]

Hubert CG, Rivera M, Spangler LC, Wu Q, Mack SC, Prager BC, Couce M, McLendon RE, Sloan AE, and Rich JN (2016). A Three-Dimensional Organoid Culture System Derived from Human Glioblastomas Recapitulates the Hypoxic Gradients and Cancer Stem Cell Heterogeneity of Tumors Found In Vivo. Cancer Res. 76, 2465–2477. [PubMed: 26896279]

Johnson LA, Scholler J, Ohkuri T, Kosaka A, Patel PR, McGettigan SE, Nace AK, Dentchev T, Thekkat P, Loew A, et al. (2015). Rational development and characterization of humanized anti-EGFR variant III chimeric antigen receptor T cells for glioblastoma. Sci. Transl. Med 7, 275ra22.

June CH, O'Connor RS, Kawalekar OU, Ghassemi S, and Milone MC (2018). CAR T cell immunotherapy for human cancer. Science 359, 1361–1365. [PubMed: 29567707]

Kadoshima T, Sakaguchi H, Nakano T, Soen M, Ando S, Eiraku M, and Sasai Y (2013). Self-organization of axial polarity, inside-out layer pattern, and species-specific progenitor dynamics in human ES cell-derived neocortex. Proc. Natl. Acad. Sci. USA 110, 20284–20289. [PubMed: 24277810]

Kelly PJ, Daumas-Duport C, Scheithauer BW, Kall BA, and Kispert DB (1987). Stereotactic histologic correlations of computed tomography- and magnetic resonance imaging-defined abnormalities in patients with glial neoplasms. Mayo Clin. Proc 62, 450–459. [PubMed: 3553757]

Kim S, Scheffler K, Halpern AL, Bekritsky MA, Noh E, Kallberg M, Chen X, Kim Y, Beyter D, Krusche P, and Saunders CT (2018). Strelka2: fast and accurate calling of germline and somatic variants. Nat. Methods 15, 591–594. [PubMed: 30013048]

Koboldt DC, Zhang Q, Larson DE, Shen D, McLellan MD, Lin L, Miller CA, Mardis ER, Ding L, and Wilson RK (2012). VarScan 2: somatic mutation and copy number alteration discovery in cancer by exome sequencing. Genome Res. 22, 568–576. [PubMed: 22300766]

Kopper O, de Witte CJ, Lõhmussaar K,Valle-Inclan JE, Hami N, Kester L, Balgobind AV, Korving J, Proost N, Begthel H, et al. (2019). An organoid platform for ovarian cancer captures intra-and interpatient heterogeneity. Nat. Med 25, 838–849. [PubMed: 31011202]

Krueger DA, Care MM, Holland K, Agricola K, Tudor C, Mangeshkar P, Wilson KA, Byars A, Sahmoud T, and Franz DN (2010). Everolimus for subependymal giant-cell astrocytomas in tuberous sclerosis. N. Engl. J. Med 363, 1801–1811. [PubMed: 21047224]

Kuan CT, Wakiya K, Dowell JM, Herndon JE 2nd, Reardon DA, Graner MW, Riggins GJ, Wikstrand CJ, and Bigner DD (2006). Glycoprotein nonmetastatic melanoma protein B, a potential molecular therapeutic target in patients with glioblastoma multiforme. Clin. Cancer Res 12, 1970–1982. [PubMed: 16609006]

Kuleshov MV, Jones MR, Rouillard AD, Fernandez NF, Duan Q, Wang Z, Koplev S, Jenkins SL, Jagodnik KM, Lachmann A, et al. (2016). Enrichr: a comprehensive gene set enrichment analysis web server 2016 update. Nucleic Acids Res. 44 (W1), W90–7. [PubMed: 27141961]

Lake BB, Chen S, Sos BC, Fan J, Kaeser GE, Yung YC, Duong TE, Gao D, Chun J, Kharchenko PV, and Zhang K (2018). Integrative single-cell analysis of transcriptional and epigenetic states in the human adult brain. Nat. Biotechnol 36, 70–80. [PubMed: 29227469]

Lancaster MA, Renner M, Martin CA, Wenzel D, Bicknell LS, Hurles ME, Homfray T, Penninger JM, Jackson AP, and Knoblich JA (2013). Cerebral organoids model human brain development and microcephaly. Nature 501, 373–379. [PubMed: 23995685]

Landrum MJ, Lee JM, Benson M, Brown G, Chao C, Chitipiralla S, Gu B, Hart J, Hoffman D, Hoover J, et al. (2016). ClinVar: public archive of interpretations of clinically relevant variants. Nucleic Acids Res. 44 (D1), D862–D868. [PubMed: 26582918]

Ledur PF, Onzi GR, Zong H, and Lenz G (2017). Culture conditions defining glioblastoma cells behavior: what is the impact for novel discoveries? Oncotarget 8, 69185–69197. [PubMed: 28978189]

Lee J, Kotliarova S, Kotliarov Y, Li A, Su Q, Donin NM, Pastorino S, Purow BW, Christopher N, Zhang W, et al. (2006). Tumor stem cells derived from glioblastomas cultured in bFGF and EGF more closely mirror the phenotype and genotype of primary tumors than do serum-cultured cell lines. Cancer Cell 9, 391–403. [PubMed: 16697959]

Lee SH, Hu W, Matulay JT, Silva MV, Owczarek TB, Kim K, Chua CW, Barlow LJ, Kandoth C, Williams AB, et al. (2018). Tumor Evolution and Drug Response in Patient-Derived Organoid Models of Bladder Cancer. Cell 173, 515–528. [PubMed: 29625057]

Leek JT, Johnson WE, Parker HS, Jaffe AE, and Storey JD (2012). The sva package for removing batch effects and other unwanted variation in high-throughput experiments. Bioinformatics 28, 882–883. [PubMed: 22257669]

Li H (2011).A statistical framework for SNP calling, mutation discovery, association mapping and population genetical parameter estimation from sequencing data. Bioinformatics 27, 2987–2993. [PubMed: 21903627]

Li H, and Durbin R (2009). Fast and accurate short read alignment with Burrows-Wheeler transform. Bioinformatics 25, 1754–1760. [PubMed: 19451168]

Li H, Handsaker B, Wysoker A, Fennell T, Ruan J, Homer N, Marth G, Abecasis G, and Durbin R; 1000 Genome Project Data Processing Subgroup (2009). The Sequence Alignment/Map format and SAMtools. Bioinformatics 25, 2078–2079. [PubMed: 19505943]

Liao Y, Smyth GK, and Shi W (2019). The R package Rsubread is easier, faster, cheaper and better for alignment and quantification of RNA sequencing reads. Nucleic Acids Res. 47, e47. [PubMed: 30783653]

Linkous A, Balamatsias D, Snuderl M, Edwards L, Miyaguchi K, Milner T, Reich B, Cohen-Gould L, Storaska A, Nakayama Y, et al. (2019). Modeling Patient-Derived Glioblastoma with Cerebral Organoids. Cell Rep. 26, 3203–3211. [PubMed: 30893594]

Liu X, Jian X, and Boerwinkle E (2011). dbNSFP: a lightweight database of human nonsynonymous SNPs and their functional predictions. Hum. Mutat 32, 894–899. [PubMed: 21520341]

Liu X, Wu C, Li C, and Boerwinkle E (2016). dbNSFP v3.0: A One-Stop Database of Functional Predictions and Annotations for Human Nonsynonymous and Splice-Site SNVs. Hum. Mutat 37, 235–241. [PubMed: 26555599]

Love MI, Huber W, and Anders S (2014). Moderated estimation of fold change and dispersion for RNA-seq data with DESeq2. Genome Biol. 15, 550. [PubMed: 25516281]

Macosko EZ, Basu A, Satija R, Nemesh J, Shekhar K, Goldman M, Tirosh I, Bialas AR, Kamitaki N, Martersteck EM, et al. (2015). Highly Parallel Genome-wide Expression Profiling of Individual Cells Using Nanoliter Droplets. Cell 161, 1202–1214. [PubMed: 26000488]

Mandel JJ, Yust-Katz S, Patel AJ, Cachia D, Liu D, Park M, Yuan Y, Kent TA, and de Groot JF (2018). Inability of positive phase II clinical trials of investigational treatments to subsequently predict positive phase III clinical trials in glioblastoma. Neuro-oncol. 20, 113–122. [PubMed: 29016865]

Mansour AA, Goncalves JT, Bloyd CW, Li H, Fernandes S, Quang D, Johnston S, Parylak SL, Jin X, and Gage FH (2018). An in vivo model of functional and vascularized human brain organoids. Nat. Biotechnol 36, 432–441. [PubMed: 29658944]

McKenna A, Hanna M, Banks E, Sivachenko A, Cibulskis K, Kernytsky A, Garimella K, Altshuler D, Gabriel S, Daly M, and DePristo MA (2010). The Genome Analysis Toolkit: a MapReduce framework for analyzing next-generation DNA sequencing data. Genome Res. 20, 1297–1303. [PubMed: 20644199]

Mellinghoff IK, Wang MY, Vivanco I, Haas-Kogan DA, Zhu S, Dia EQ, Lu KV, Yoshimoto K, Huang JH, Chute DJ, et al. (2005). Molecular determinants of the response of glioblastomas to EGFR kinase inhibitors. N. Engl. J. Med 353, 2012–2024. [PubMed: 16282176]

Neal JT, Li X, Zhu J, Giangarra V, Grzeskowiak CL, Ju J, Liu IH, Chiou SH, Salahudeen AA, Smith AR, et al. (2018). Organoid Modeling of the Tumor Immune Microenvironment. Cell 175, 1972–1988. [PubMed: 30550791]

Neftel C, Laffy J, Filbin MG, Hara T, Shore ME, Rahme GJ, Richman AR, Silverbush D, Shaw ML, Hebert CM, et al. (2019). An Integrative Model of Cellular States, Plasticity, and Genetics for Glioblastoma. Cell 178, 835–849. [PubMed: 31327527]

Newick K, O'Brien S, Moon E, and Albelda SM (2017). CAR T Cell Therapy for Solid Tumors. Annu. Rev. Med 68, 139–152. [PubMed: 27860544]

O'Rourke DM, Nasrallah MP, Desai A, Melenhorst JJ, Mansfield K, Morrissette JJD, Martinez-Lage M, Brem S, Maloney E, Shen A, et al. (2017). A single dose of peripherally infused EGFRvIII-directed CAR T cells mediates antigen loss and induces adaptive resistance in patients with recurrent glioblastoma. Sci. Transl. Med 9, eaaa0984. [PubMed: 28724573]

Ogawa J, Pao GM, Shokhirev MN, and Verma IM (2018). Glioblastoma Model Using Human Cerebral Organoids. Cell Rep. 23, 1220–1229. [PubMed: 29694897]

Ostrom QT, Gittleman H, Truitt G, Boscia A, Kruchko C, and Barnholtz-Sloan JS (2018). CBTRUS Statistical Report: Primary Brain and Other Central Nervous System Tumors Diagnosed in the United States in 2011-2015. Neuro-oncol. 20 (suppl_4), iv1–iv86. [PubMed: 30445539]

Pandita A, Aldape KD, Zadeh G, Guha A, and James CD (2004). Contrasting in vivo and in vitro fates of glioblastoma cell subpopulations with amplified EGFR. Genes Chromosomes Cancer 39, 29–36. [PubMed: 14603439]

Paolillo M, Boselli C, and Schinelli S (2018). Glioblastoma under Siege: An Overview of Current Therapeutic Strategies. Brain Sci. 8, E15. [PubMed: 29337870]

Paşca AM, Sloan SA, Clarke LE,Tian Y, Makinson CD, Huber N, Kim CH, Park JY, O'Rourke NA, Nguyen KD, et al. (2015). Functional cortical neurons and astrocytes from human pluripotent stem cells in 3D culture. Nat. Methods 12, 671–678. [PubMed: 26005811]

Patel AP, Tirosh I, Trombetta JJ, Shalek AK, Gillespie SM, Wakimoto H, Cahill DP, Nahed BV, Curry WT, Martuza RL, et al. (2014). Single-cell RNA-seq highlights intratumoral heterogeneity in primary glioblastoma. Science 344, 1396–1401. [PubMed: 24925914]

Patrizii M, Bartucci M, Pine SR, and Sabaawy HE (2018). Utility of Glioblastoma Patient-Derived Orthotopic Xenografts in Drug Discovery and Personalized Therapy. Front. Oncol 8, 23. [PubMed: 29484285]

Porter DL, Levine BL, Kalos M, Bagg A, and June CH (2011). Chimeric antigen receptor-modified T cells in chronic lymphoid leukemia. N. Engl. J. Med 365, 725–733. [PubMed: 21830940]

Qian X, Nguyen HN, Song MM, Hadiono C, Ogden SC, Hammack C, Yao B, Hamersky GR, Jacob F, Zhong C, et al. (2016). Brain-Region-Specific Organoids Using Mini-bioreactors for Modeling ZIKV Exposure. Cell 165, 1238–1254. [PubMed: 27118425]

Rich JN, Reardon DA, Peery T, Dowell JM, Quinn JA, Penne KL, Wikstrand CJ, Van Duyn LB, Dancey JE, McLendon RE, et al. (2004). Phase II trial of gefitinib in recurrent glioblastoma. J. Clin. Oncol 22, 133–142. [PubMed: 14638850]

Robinson JT, Thorvaldsdóttir H, Winckler W, Guttman M, Lander ES, Getz G, and Mesirov JP (2011). Integrative genomics viewer. Nat. Biotechnol 29, 24–26. [PubMed: 21221095]

Roldán GB, Scott JN, McIntyre JB, Dharmawardene M, de Robles PA, Magliocco AM, Yan ES, Parney IF, Forsyth PA, Cairncross JG, et al. (2009). Population-based study of pseudoprogression after chemoradiotherapy in GBM. Can. J. Neurol. Sci 36, 617–622.

Sachs N, de Ligt J, Kopper O, Gogola E, Bounova G, Weeber F, Balgobind AV, Wind K, Gracanin A, Begthel H, et al. (2018). A Living Biobank of Breast Cancer Organoids Captures Disease Heterogeneity. Cell 172, 373–386. [PubMed: 29224780]

Saunders A, Macosko EZ, Wysoker A, Goldman M, Krienen FM, de Rivera H, Bien E, Baum M, Bortolin L, Wang S, et al. (2018). Molecular Diversity and Specializations among the Cells of the Adult Mouse Brain. Cell 174, 1015–1030. [PubMed: 30096299]

Shi L, Yang X, Froelich CJ, and Greenberg AH (2000). Purification and use of granzyme B. Methods Enzymol. 322, 125–143. [PubMed: 10914010]

Stuart T, Butler A, Hoffman P, Hafemeister C, Papalexi E, Mauck WM, Stoeckius M, Smibert P, and Satija R (2019). Comprehensive integration of single cell data. Cell 177, 1888–1902. [PubMed: 31178118]

Stupp R, Mason WP, van den Bent MJ, Weller M, Fisher B, Taphoorn MJ, Belanger K, Brandes AA, Marosi C, Bogdahn U, et al. European Organisation for Research and Treatment of Cancer Brain Tumor and Radiotherapy Groups; National Cancer Institute of Canada Clinical Trials Group (2005). Radiotherapy plus concomitant and adjuvant temozolomide for glioblastoma. N. Engl. J. Med 352, 987–996. [PubMed: 15758009]

Subramanian A, Tamayo P, Mootha VK, Mukherjee S, Ebert BL, Gillette MA, Paulovich A, Pomeroy SL, Golub TR, Lander ES, and Mesirov JP (2005). Gene set enrichment analysis: a knowledge-based approach for interpreting genome-wide expression profiles. Proc. Natl. Acad. Sci. USA 102, 15545–15550. [PubMed: 16199517]

Sun GJ, Zhou Y, Stadel RP, Moss J, Yong JH, Ito S, Kawasaki NK, Phan AT, Oh JH, Modak N, et al. (2015). Tangential migration of neuronal precursors of glutamatergic neurons in the adult mammalian brain. Proc. Natl. Acad. Sci. USA 112, 9484–9489. [PubMed: 26170290]

Tirosh I, Venteicher AS, Hebert C, Escalante LE, Patel AP, Yizhak K, Fisher JM, Rodman C, Mount C, Filbin MG, et al. (2016). Single-cell RNA-seq supports a developmental hierarchy in human oligodendroglioma. Nature 539, 309–313. [PubMed: 27806376]

Uhm JH, Ballman KV, Wu W, Giannini C, Krauss JC, Buckner JC, James CD, Scheithauer BW, Behrens RJ, Flynn PJ, et al. (2011). Phase II evaluation of gefitinib in patients with newly diagnosed Grade 4 astrocytoma: Mayo/North Central Cancer Treatment Group Study N0074. Int. J. Radiat. Oncol. Biol. Phys 80, 347–353. [PubMed: 20510539]

Van der Auwera GA, Carneiro MO, Hartl C, Poplin R, Del Angel G, Levy-Moonshine A, Jordan T, Shakir K, Roazen D, Thibault J, et al. (2013). From FastQ data to high confidence variant calls: the Genome Analysis Toolkit best practices pipeline. Curr. Protoc. Bioinformatics 43, 11.10.1–11.10.33. [PubMed: 25431634]

Varia MA, Calkins-Adams DP, Rinker LH, Kennedy AS, Novotny DB, Fowler WC Jr., and Raleigh JA (1998). Pimonidazole: a novel hypoxia marker for complementary study of tumor hypoxia and cell proliferation in cervical carcinoma. Gynecol. Oncol 71, 270–277. [PubMed: 9826471]

Venteicher AS, Tirosh I, Hebert C, Yizhak K, Neftel C, Filbin MG, Hovestadt V, Escalante LE, Shaw ML, Rodman C, et al. (2017). Decoupling genetics, lineages, and microenvironment in IDH-mutant gliomas by single-cell RNA-seq. Science 355, eaai8478. [PubMed: 28360267]

Wang K, Li M, and Hakonarson H (2010). ANNOVAR: functional annotation of genetic variants from high-throughput sequencing data. Nucleic Acids Res. 38, e164. [PubMed: 20601685]

Weng YL, An R, Cassin J, Joseph J, Mi R, Wang C, Zhong C, Jin SG, Pfeifer GP, Bellacosa A, et al. (2017). An Intrinsic Epigenetic Barrier for Functional Axon Regeneration. Neuron 94, 337–346. [PubMed: 28426967]

Yan HHN, Siu HC, Law S, Ho SL, Yue SSK, Tsui WY, Chan D, Chan AS, Ma S, Lam KO, et al. (2018). A Comprehensive Human Gastric Cancer Organoid Biobank Captures Tumor Subtype Heterogeneity and Enables Therapeutic Screening. Cell Stem Cell 23, 882–897. [PubMed: 30344100]

Highlights

- Rapid establishment of glioblastoma organoids (GBOs) in a defined medium with biobank
- GBOs maintain parental tumor cellular heterogeneity, gene expression, and mutations
- GBO transplantation exhibits efficient engraftment and aggressive infiltration
- Tumor-specific treatment responses in GBOs to drugs and CAR-T cells

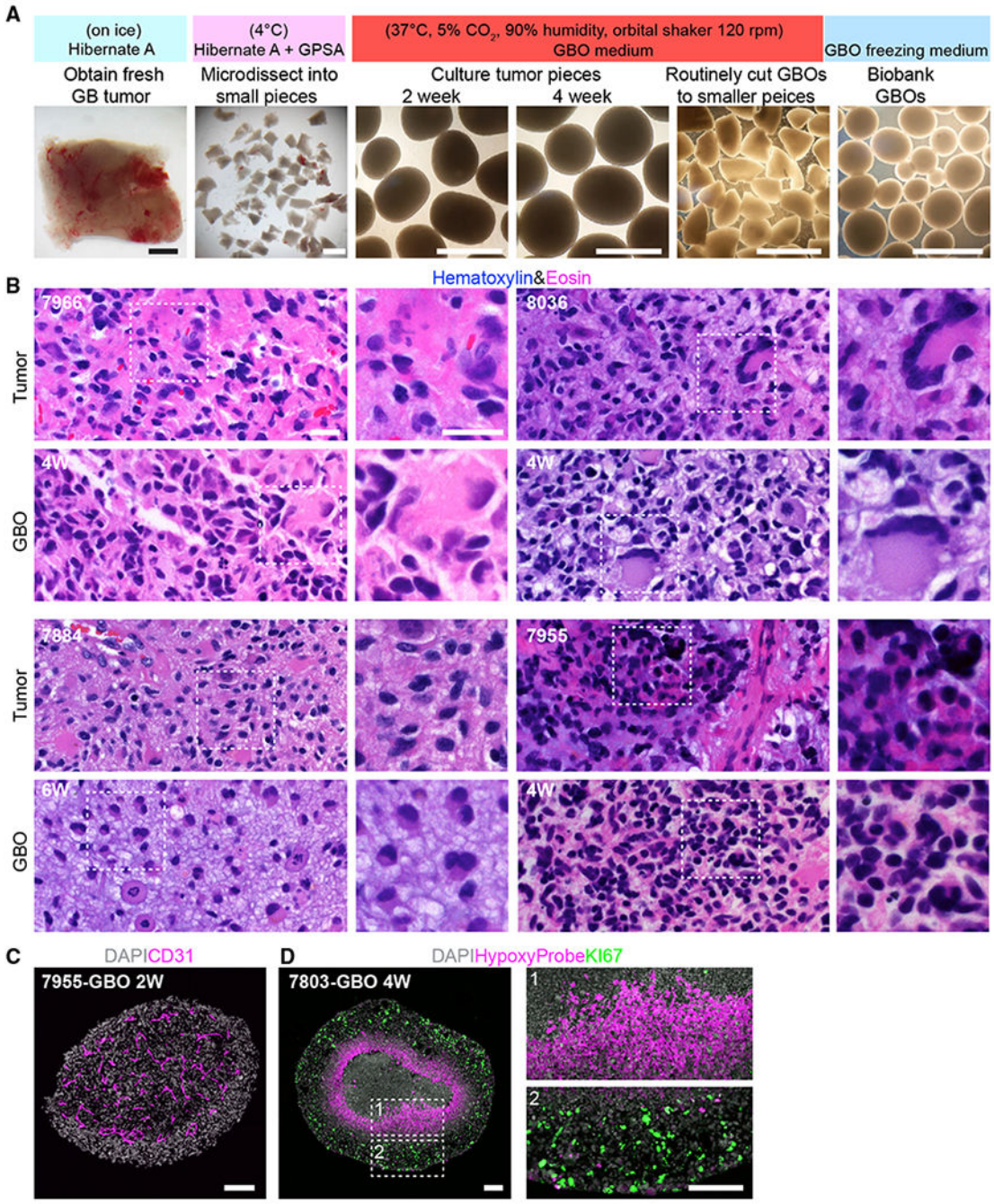

Figure 1. Generation of GBOs that Retain Histologic Features of Parental Tumors

(A) A schematic of the procedure with sample bright-field images. Scale bar, 1 mm.

(B) Sample H&E staining images of parental tumors and corresponding GBOs. Age of GBOs in weeks (W) is listed. Scale bars, 20 μm.

(C) Sample confocal image of micro-vasculature retained in GBO with immunostaining for CD31. Scale bar, 100 μm.

(D) Sample confocal images showing the hypoxia gradient present in a large GBO with immunostaining for HypoxyProbe and KI67. Insets highlight $KI67^{+}$ proliferating cells at the periphery (box 2), but not in the hypoxic core (box 1). Scale bars, 100 μm.
See also Figure S2 and Tables S1 and S2.

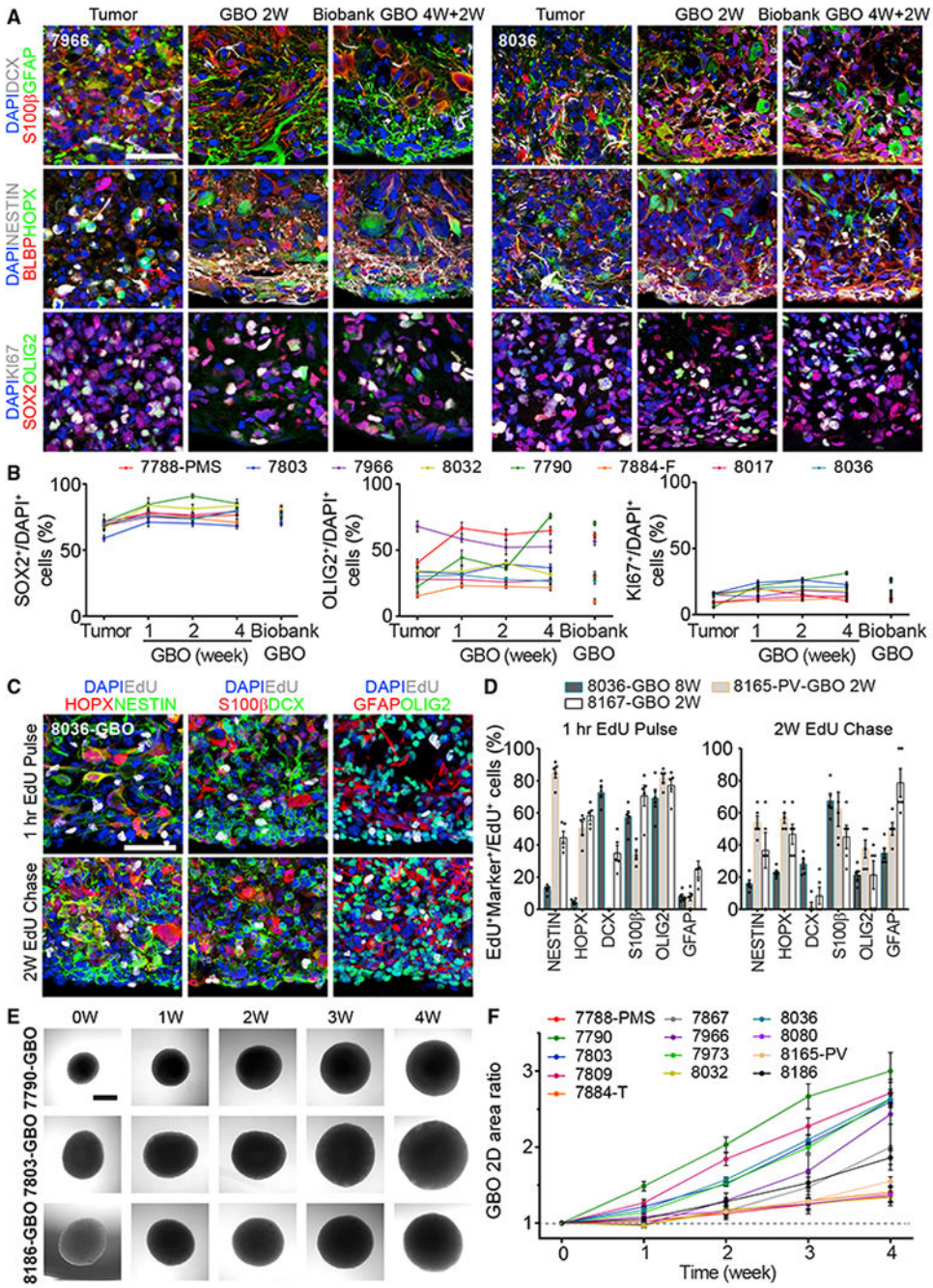

Figure 2. GBOs Retain and Continuously Generate Heterogeneous Cell Populations

(A) Sample confocal images of immunostaining for different markers showing the maintenance of parental tumor cell populations in cultured GBOs and GBOs recovered from the biobank for two patients. See Figure S1A for additional samples. Scale bar, 50 μm.

(B) Quantifications of $SOX2^+$, $OLIG2^+$, and $KI67^+$ cells in 8 parental tumors, corresponding GBOs for different culture periods, and those recovered from the biobank (4W+2W). Values represent mean ± SEM (n = 5).

(C and D) EdU pulse-chase experiments. GBOs were incubated with 1 μM EdU for 1 h and immunohistology for different markers was performed 1 h and 2 weeks later. Shown are sample confocal images (C; scale bar, 50 μm) and quantifications of $EdU^+Marker^+$ cells among EdU^+ cells after 1-h EdU pulse and 2-week EdU chase (D). Dots represent data from individual GBOs and bar values represent mean ± SEM (n = 5).

(E and F) Growth of biobanked GBOs after recovery. Shown are sample bright-field images of individual GBOs recovered from the biobank (E; scale bar, 500 μm) and quantification of the ratio of the measured 2D area at each time point to the 2D area at time point 0 for the same GBOs recovered from the biobank (F). Values represent mean ± SEM (n = 10 GBOs per sample).

See also Figures S1 and S2 and Tables S1 and S2.

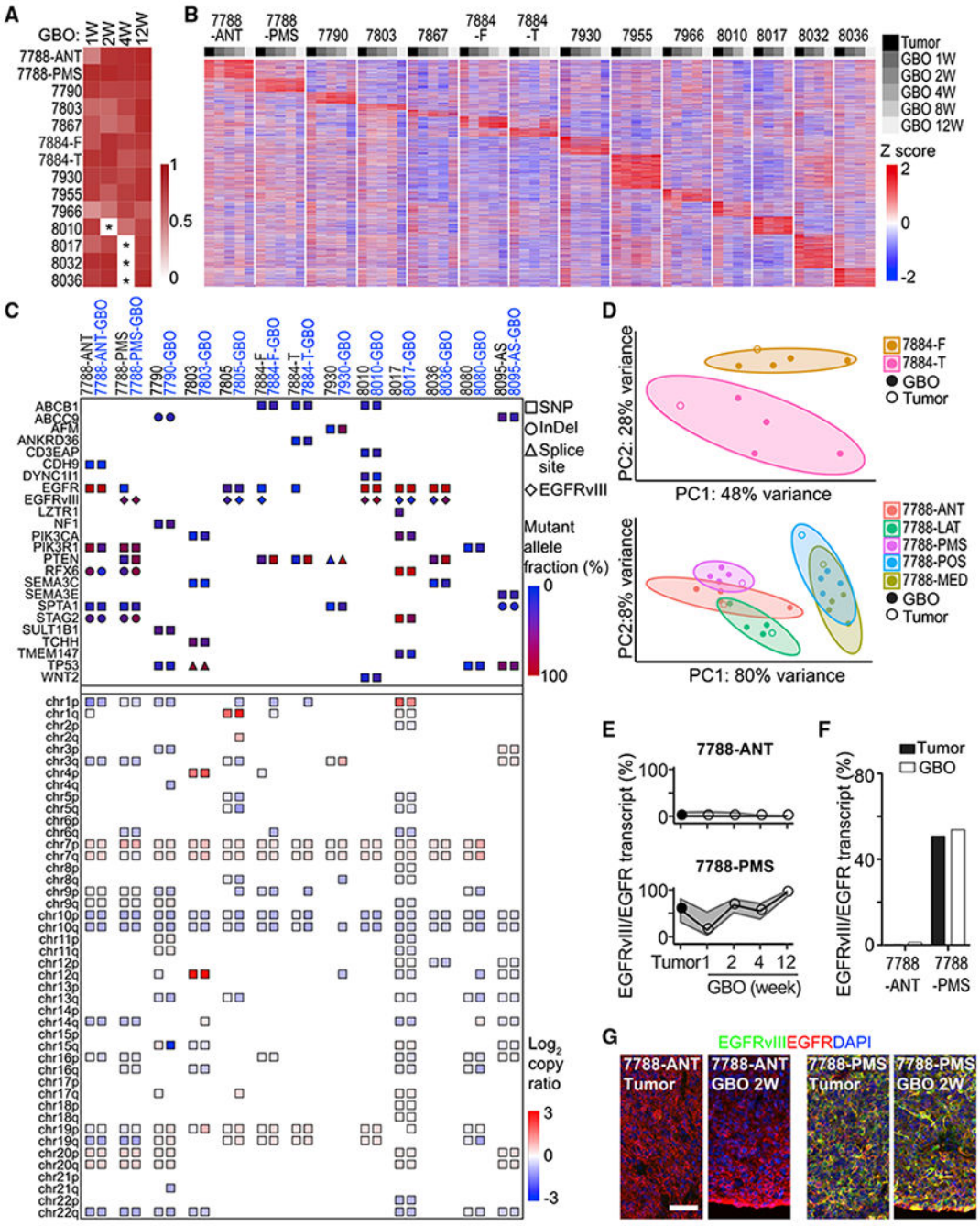

Figure 3. GBOs Maintain Inter- and Intra-tumoral Heterogeneity of Gene Expression and Mutational Profiles of Corresponding Parental Tumors

(A) Heatmap of transcriptome-wide gene expression Pearson correlations between parental tumors and corresponding GBOs as determined by RNA-seq. *Unsampled time points.

(B) Gene expression heatmap of the top 10,000 most variably expressed genes in parental tumors.

(C) Somatic variants in glioblastoma-associated genes (top panels) and copy number variations in autosomal chromosomal arms (bottom panels) identified by whole-exome sequencing of parental tumors, derived GBOs at 2 weeks and corresponding blood samples.

The types of variants and allele frequencies are listed (see Table S3). The *EGFRvIII* mutation was determined by RNA-seq.

(D) RNA-seq gene expression PCA plots of subregional samples for parental tumors and corresponding GBOs for different culture periods for two patients with 90% confidence ellipses.

(E) *EGFRvIII* transcript abundance relative to EGFR as determined by RNA-seq in parental tumors and corresponding GBOs with 95% credible intervals.

(F) *EGFRvIII* transcript abundance relative to EGFR as determined by digital PCR in parental tumors and corresponding GBOs at 2 weeks.

(G) Confocal images of EGFRvIII and EGFR immunostaining and DAPI for parental tumors and corresponding GBOs. Scale bar, 50 μm.

See also Figure S3 and Tables S1, S2, and S3.

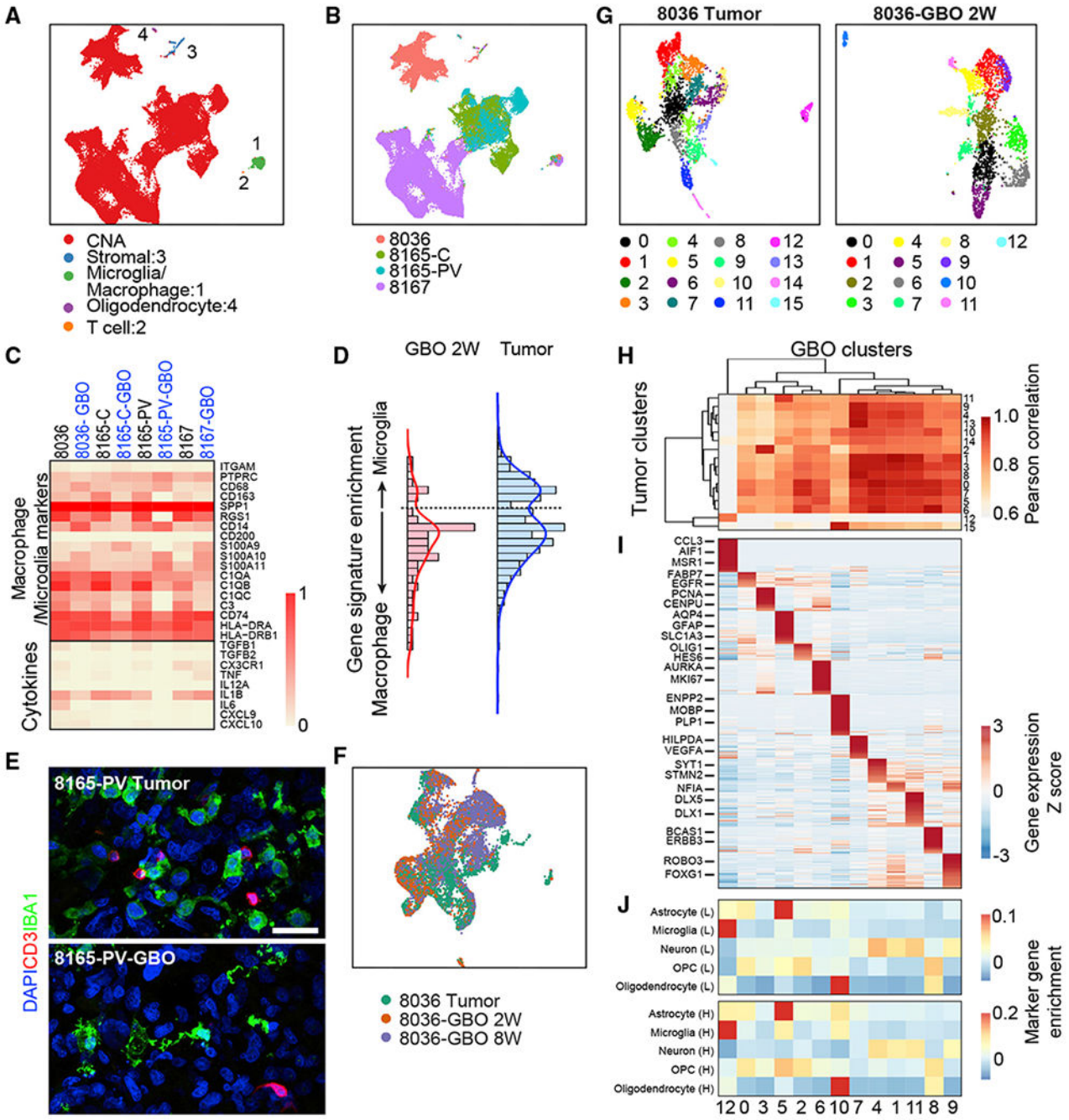

Figure 4. Single-Cell RNA-Seq Analyses of Parental Tumors and Corresponding GBOs

(A) UMAP plot of single-cell RNA expression from UP-8036, UP-8165-C, UP-8165-PV, and UP-8167 parental tumors and corresponding GBOs. Neoplastic cells are identified and colored by the presence of CNAs (see Figure S4A). Non-neoplastic cell clusters shared by cells from different patients and corresponding GBOs are colored and marked: 1 (microphage/microglia cluster), 2 (T cell cluster), 3 (stromal cell cluster), and 4 (mature oligodendrocyte cluster).

(B) UMAP plot of single-cell RNA expression from four parental tumors and corresponding GBOs. Cells are colored by patients and subregions.
(C) Heatmap of gene expression of selected macrophage/microglia marker genes and cytokines in the macrophage/microglia cell cluster (1 in A).
(D) Histogram of microglia versus macrophage gene signature expression in cells from the macrophage/microglia cell population from all parental tumors and all GBOs at 2 weeks.
(E) Confocal images of immunostaining for microphage/microglia marker IBA1 and T cell marker CD3 in the parental tumor and corresponding GBO at 2 weeks. Scale bar, 50 μm.
(F) UMAP plot of UP-8036 parental tumor and GBOs at 2 and 8 weeks colored by samples.
(G) UMAP plots of UP-8036 parental tumor and GBOs at 2 weeks colored by cluster. The same cluster number is listed in (H) and (J).
(H) Heatmap of gene expression Pearson correlation of clusters identified in the UP-8036 parental tumor (rows) and GBOs at 2 weeks (columns) with hierarchical clustering by Euclidian distance.
(I) Heatmap of gene expression of cluster-specific markers in UP-8036-GBOs with columns corresponding to (H). See Table S4 for the detailed gene list.
(J) Comparison of cell clusters in UP-8036 GBOs at 2 weeks (corresponding to that in H) with normal adult brain cells identified by single-nuclei RNA-seq of human adult brains in Lake et al. (2018) (L, top panel) and Habib et al. (2017) (H, bottom panel) with marker gene enrichment analysis. OPC, oligodendrocyte precursor cell.
See also Figure S4 and Tables S1, S2, and S4.

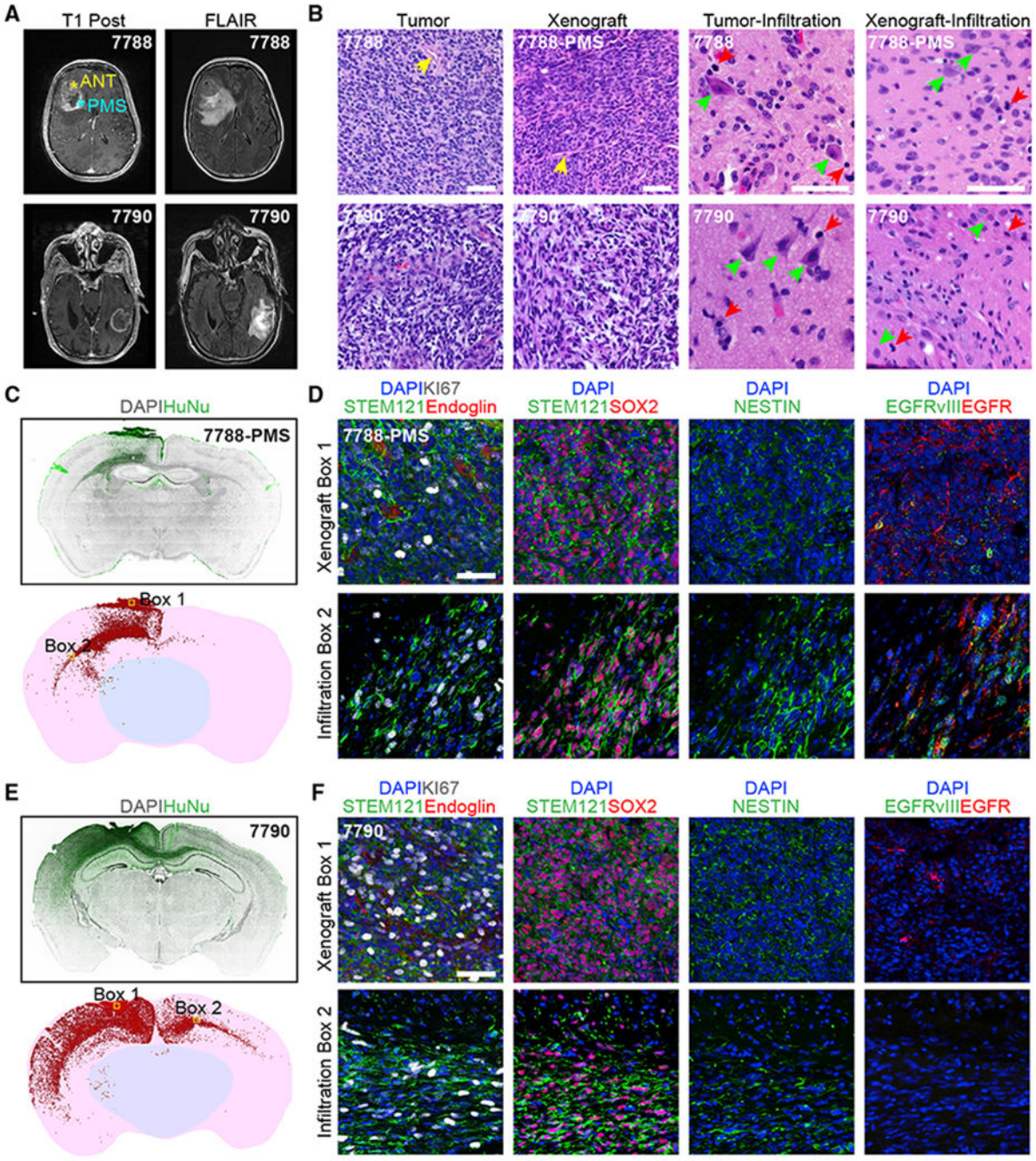

Figure 5. Orthotopic Transplantation of GBOs into Adult Immunodeficient Mice Displays Efficient Engraftment and Extensive Infiltration into the Brain Parenchyma

(A) MRI T1 post-contrast (left) and FLAIR (right) patient brain images.

(B) Sample H&E staining images of the tumor bulk versus infiltrated areas of parental patient tissues and the original xenograft sites and infiltrated areas for corresponding GBOs at 2 months post-transplantation. Prominent blood vessels (yellow arrow heads) are observed in both the tumor bulk in patients and original GBO xenograft sites in mice. Infiltrated areas are shown with human neurons and mouse neurons (green arrow heads) and tumor cells (red arrow heads), respectively. Scale bar, 100 μm.

(C and D) Xenograft of UP-7788-PMS-GBO at 2 months post-transplantation. (C) Coronal section views of human nuclear antigen (HuNu) immunostaining (top) and reconstruction for quantification of infiltrated cells (bottom). Each red dot represents a $HuNu^+$ cell. (D) Sample confocal images of areas in box 1 and 2 in (C, bottom panel) for immunostaining of human-specific cytoplasmic antigen (STEM121) showing the extensive vascularization from the host (endoglin immunostaining) in the original xenograft site, and proliferation (KI67 immunostaining), progenitor (SOX2, NESTIN immunostaining), and EGFR/mutant EGFRvIII expression status of tumor cells in the original xenograft site (box 1) and the infiltrated area (box 2). Scale bar, 50 μm.

(E and F) Xenograft of UP-7790-GBO at 2 months post-transplantation. Cornal section image and reconstruction (E) and sample confocal images in box 1 and 2 (F) are similar as in (C) and (D).

See also Figure S5, Tables S1, S2, and S5, and Video S1.

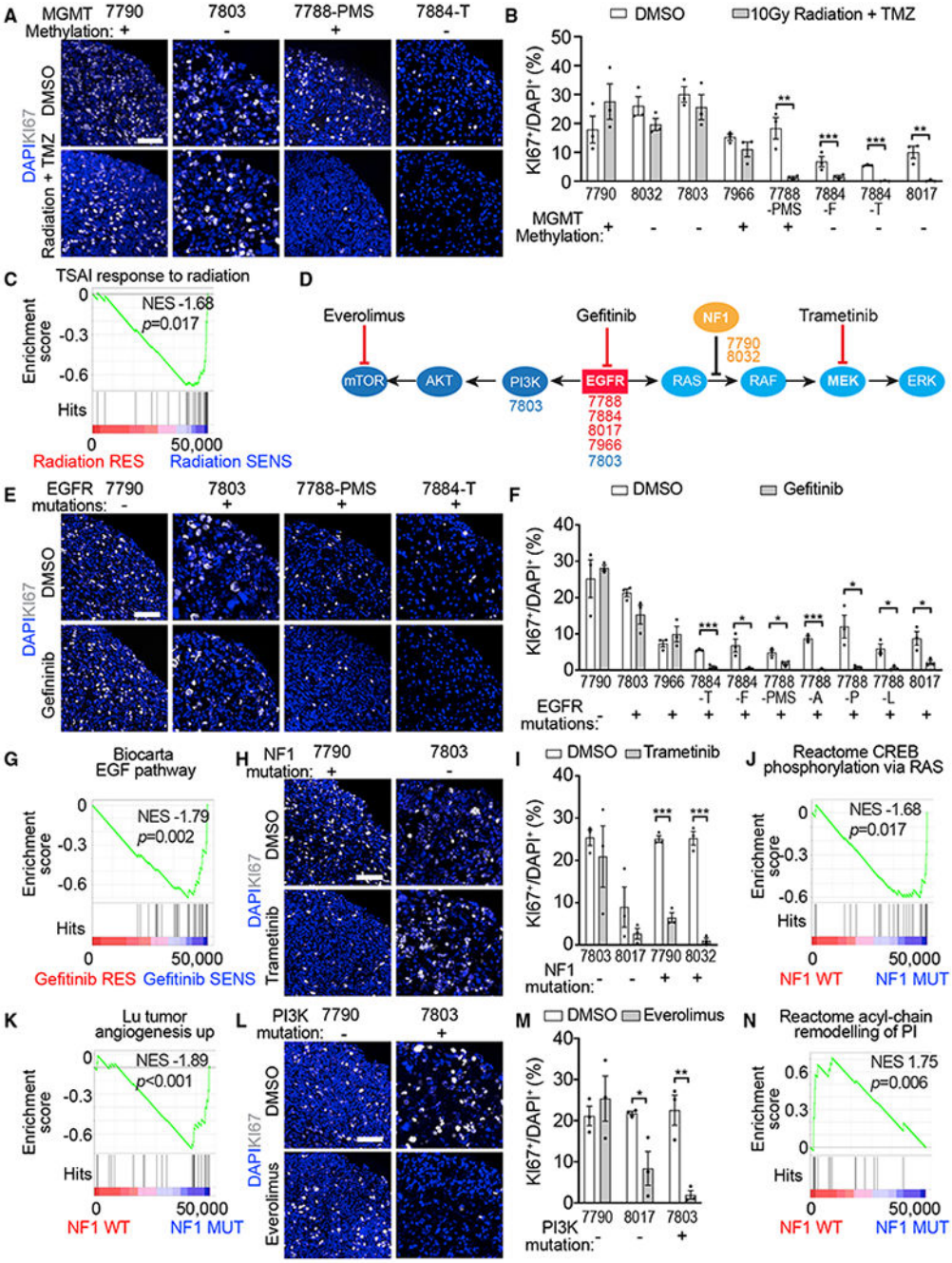

Figure 6. Therapeutic Testing of GBOs *In Vitro*

(A–C) Treatment of GBOs with 10 Gy radiation and temozolomide (TMZ; 50 μM). (A) Sample confocal images of KI67 immunostaining and DAPI staining. Scale bar, 100 μm. The *MGMT* methylation status identified in each parental tumor is listed. (B) Quantification of percentages of $KI67^+$ cells among $DAPI^+$ cells. See Table S6 for the age of GBOs used in the analysis. Dots represent individual data points and bar values represent mean ± SEM (n = 3; *p < 0.05; **p < 0.01; ***p < 0.001; Student's t test). (C) Gene set enrichment in

GBOs with significant reduction of $KI67^+$ cells following radiation and temozolomide treatment.

(D) Schematic of targeted treatment strategy showing genetic pathways, location of tumor-specific mutations, and mechanism of action of targeted treatments. The mutations were based on identifications in patient tumor samples via clinical sequencing (see Table S1).

(E–G) Treatment of GBOs with gefitinib (5 μM). Sample images (E) and quantification (F) are similar as in (A) and (B). Shown in (G) is gene set enrichment in samples with significant reduction of $KI67^+$ cells following gefitinib treatment.

(H–K) Treatment of GBOs with trametinib (1 μM). Sample image (H) and quantification (J) are similar as in (A) and (B). Also shown are gene set enrichment in samples with *NF1* mutations (J and K).

(L–N) Treatment of GBOs with everolimus (1 μM). Sample images (L) and quantification (M) are similar as in (A) and (B). Shown in (N) is gene set enrichment in samples without *NF1* mutations.

See also Figure S6 and Tables S1, S2, and S6.

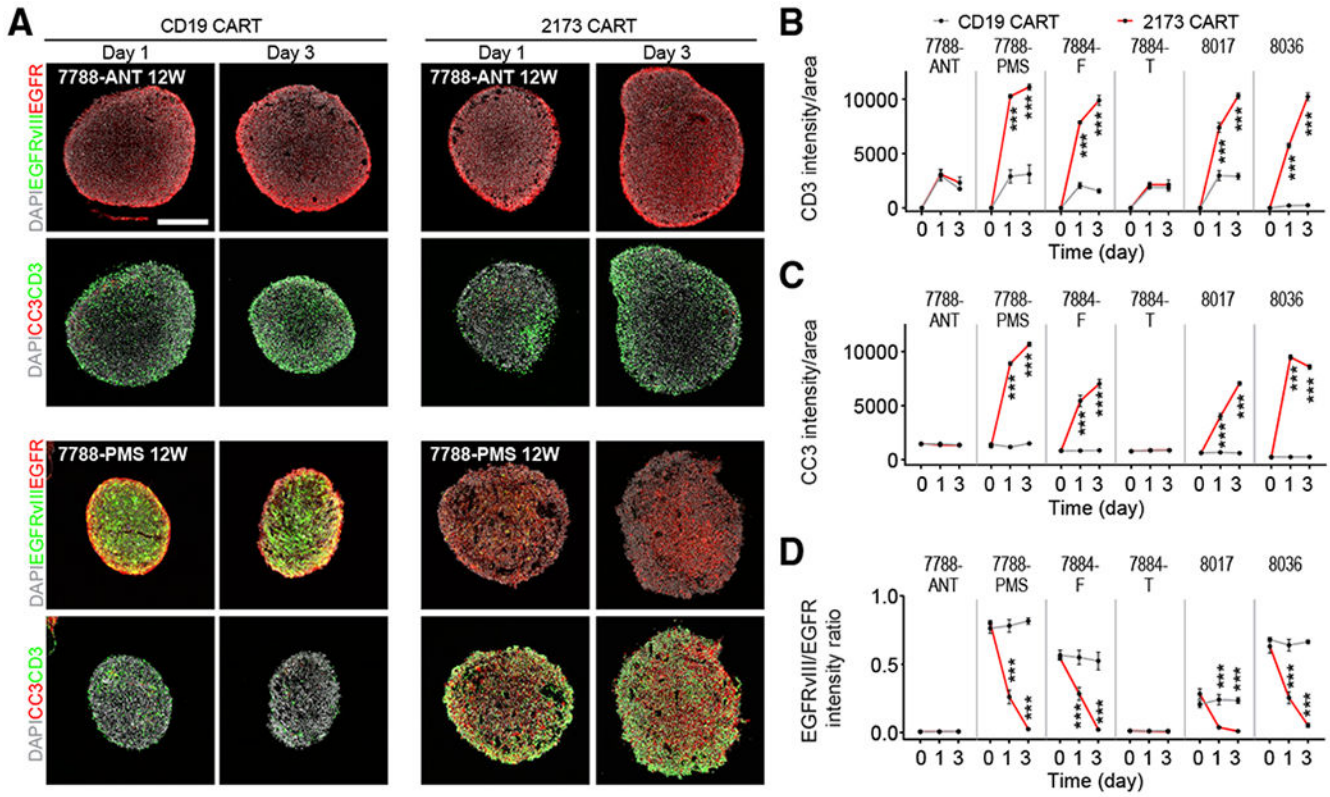

Figure 7. Modeling Immunotherapy with Co-cultures of CAR-T Cells and GBOs

(A) Sample confocal images of immunostaining of EGFR, EGFRvIII, cleaved-caspase-3 (CC3), and CD3 after 1 and 3 days of co-culture with either CD19 or 2173BBz CAR-T cells. Scale bar, 200 μm.

(B–D) Summary of quantifications of averaged signal intensity of CD3 (B), CC3 (C), and averaged EGFRvIII/EGFR signal intensity ratio (D) in GBOs after co-culture with either CD19 or 2173BBz CAR-T cells. Values represent mean ± SEM (n = 3; ***p < 0.001; two-way ANOVA with uncorrected Fisher LSD test).

See also Figure S7 and Tables S1 and S2.

KEY RESOURCES TABLE

REAGENT or RESOURCE	SOURCE	IDENTIFIER
Antibodies		
Goat polyclonal anti-Doublecortin (C-18)	Santa Cruz Biotechnology	Cat# sc-8066; RRID: AB_2088494
Goat polyclonal anti-Endoglin/CD105	R&D Systems	Cat# AF1320; RRID: AB_354735
Goat polyclonal anti-Nestin (C-20)	Santa Cruz Biotechnology	Cat# sc-21247; RRID: AB_650014
Goat polyclonal anti-Sox2 (Y-17)	Santa Cruz Biotechnology	Cat# sc-17320; RRID: AB_2286684
Mouse monoclonal anti-BLBP (AT1D1)	Abcam	Cat# ab131137; RRID: AB_11157091
Mouse monoclonal anti-CD3	BioLegend	Cat# 344802; RRID: AB_2043995
Mouse monoclonal anti-EGFR (H11)	Thermo Fisher Scientific	Cat# MA1-12693; RRID: AB_1074165
Mouse monoclonal anti-GFAP (GA5)	Millipore	Cat# MAB360; RRID: AB_11212597
Mouse monoclonal anti-Granzyme B	R&D Systems	Cat# MAB2906; RRID: AB_2263752
Mouse monoclonal anti-Nuclei, human (235-1)	Millipore	Cat# MAB1281; RRID: AB_94090
Mouse monoclonal anti-Ki67 (B56)	BD Biosciences	Cat# 550609; RRID: AB_39377
Mouse monoclonal anti-STEM121	Takara Bio	Cat# Y40410; RRID: AB_2801314
Mouse monoclonal anti-VWF (C-12)	Santa Cruz Biotechnology	Cat# sc-365712; RRID: AB_10842026
Rabbit polyclonal anti-CD31	Abcam	Cat# ab28364; RRID: AB_726362
Rabbit polyclonal anti-Cleaved Caspase-3 (Asp175)	Cell Signaling Technology	Cat# 9661; RRID: AB_2341188
Rabbit monoclonal anti-EGF Receptor vIII (D6T2Q)	Cell Signaling Technology	Cat# 64952; RRID: AB_2773018
Rabbit polyclonal anti-Hopx (FL-73)	Santa Cruz Biotechnology	Cat# sc-30216; RRID: AB_2120833
Rabbit polyclonal anti-Iba1	Wako	Cat# 019-19741; RRID: AB_839504
Rabbit polyclonal anti-Ki67	Abcam	Cat# ab15580; RRID: AB_443209
Rabbit monoclonal anti-Olig2	Abcam	Cat# ab109186; RRID: AB_10861310
Rabbit polyclonal anti-S100b	Sigma-Aldrich	Cat# S2644; RRID: AB_477501
Rat monoclonal anti-CD3 (CD3-12)	GeneTex	Cat# GTX11089; RRID: AB_369097
Donkey polyclonal anti-Goat IgG (H+L) Cross-Adsorbed Secondary Antibody, Alexa Fluor 488	Thermo Fisher Scientific	Cat# A-11055; RRID: AB_2534102
Donkey polyclonal anti-Goat IgG (H+L) Cross-Adsorbed Secondary Antibody, Alexa Fluor 555	Thermo Fisher Scientific	Cat# A-21432; RRID: AB_2535853
Donkey polyclonal anti-Goat IgG (H+L) Cross-Adsorbed Secondary Antibody, Alexa Fluor 647	Thermo Fisher Scientific	Cat# A-21447; RRID: AB_2535864
Donkey polyclonal anti-Mouse IgG (H+L) Highly Cross-Adsorbed Secondary Antibody, Alexa Fluor 488	Thermo Fisher Scientific	Cat# A-21202; RRID: AB_141607
Donkey polyclonal anti-Mouse IgG (H+L) Highly Cross-Adsorbed Secondary Antibody, Alexa Fluor 555	Thermo Fisher Scientific	Cat# A-31570; RRID: AB_2536180
Donkey polyclonal anti-Mouse IgG (H+L) Highly Cross-Adsorbed Secondary Antibody, Alexa Fluor 647	Thermo Fisher Scientific	Cat# A-31571; RRID: AB_162542
Donkey polyclonal anti-Rabbit IgG (H+L) Highly Cross-Adsorbed Secondary Antibody, Alexa Fluor 488	Thermo Fisher Scientific	Cat# A-21206; RRID: AB_2535792
Donkey polyclonal anti-Rabbit IgG (H+L) Highly Cross-Adsorbed Secondary Antibody, Alexa Fluor 555	Thermo Fisher Scientific	Cat# A-31572; RRID: AB_162543
Donkey polyclonal anti-Rabbit IgG (H+L) Highly Cross-Adsorbed Secondary Antibody, Alexa Fluor 647	Thermo Fisher Scientific	Cat# A-31573; RRID: AB_2536183

REAGENT or RESOURCE	SOURCE	IDENTIFIER
Donkey polyclonal anti-Rat IgG (H+L) Highly Cross-Adsorbed Secondary Antibody, Alexa Fluor 488	Thermo Fisher Scientific	Cat# A-21208; RRID: AB_2535794
Biological Samples		
Human glioblastoma tissue	Hospital of the University of Pennsylvania	https://www.pennmedicine.org
Human blood samples	Hospital of the University of Pennsylvania	https://www.pennmedicine.org
Chemicals, Peptides, and Recombinant Proteins		
1X RBC lysis buffer	Thermo Fisher Scientific	00433357
2-Mercaptoethanol	Thermo Fisher Scientific	21985023
Advantage 2 PCR Kit	Takara Bio	639206
Advantage UltraPure PCR deoxynucleotide mix (10mM each dNTP)	Takara Bio	639125
Amphotericin B	Thermo Fisher Scientific	15290026
B-27 Supplement (50X), minus vitamin A	Thermo Fisher Scientific	12587010
Bovine serum albumin (BSA)	Sigma-Aldrich	Cat# B6917; CAS# 9048-46-8
Corn oil	Sigma-Aldrich	Cat# C8267; CAS# 8001-30-7
DAPI	Sigma-Aldrich	Cat# 10236276001; CAS# 28718-90-3
Dimethyl sulfoxide (DMSO)	Sigma-Aldrich	Cat# D2650; CAS# 67-68-5
DL-Dithiothreitol solution (1 M)	Sigma-Aldrich	Cat# 43816; CAS# 3483-12-3
Dulbecco's Modified Eagle Medium/Nutrient Mixture F-12 (DMEM/F-12)	Thermo Fisher Scientific	11320033
Dulbecco's phosphate-buffered saline (DPBS), calcium, magnesium	Thermo Fisher Scientific	14040133
Dulbecco's phosphate-buffered saline (DPBS), no calcium, no magnesium	Thermo Fisher Scientific	14190144
Dynabeads Human T-Activator CD3/CD28 for T Cell Expansion and Activation	Thermo Fisher Scientific	11131D
EdU	Abcam	ab146186
Everolimus	Santa Cruz Biotechnology	Cat# sc-218452; CAS# 159351-69-6
EZ-Tn5 Transposase	Lucigen	TNP92110
Formaldehyde, 16%, methanol free, Ultra Pure	Polysciences	Cat# 18814-10; CAS#: 50-00-0
Gefitinib	Santa Cruz Biotechnology	Cat# sc-202166; CAS# 184475-35-2
Gelfoam Sponge	Pfizer	031508
GlutaMAX supplement	GIBCO	35050061
Hibernate A medium	BrainBits	HA
Human insulin solution	Sigma-Aldrich	Cat# I9278; CAS# 11061-68-0
IDT for Illumina Nextera DNA UD Indexes Set A	Illumina	20027213
Illumina Exome Panel - Enrichment Oligos	Illumina	20020183
ImmunoCult-XF T Cell Expansion Medium	StemCell Technologies	10981
KAPA HiFi DNA Polymerase with dNTPs	Kapa Biosystems	KK2102
Maxi-Cure Super Glue	Bob Smith Industries	BSI-113
MEM Non-Essential Amino Acids Solution (100X)	Thermo Fisher Scientific	11140050

REAGENT or RESOURCE	SOURCE	IDENTIFIER
$MgCl_2$ (1M)	Thermo Fisher Scientific	AM9530G
Mouse on Mouse (M.O.M.) Blocking Reagent	Vector Laboratories	MKB-2213
N-2 Supplement (100X)	Thermo Fisher Scientific	17502048
Neurobasal medium	Thermo Fisher Scientific	21103049
Nextera DNA Flex Pre-Enrichment Library Prep and Enrichment Reagents	Illumina	20025523
Nuclease-Free Water (not DEPC-Treated)	Thermo Fisher Scientific	AM9937
Penicillin-Streptomycin (5,000 U/mL)	Thermo Fisher Scientific	15070063
Polyethylene glycol solution, 40%	Sigma-Aldrich	P1458
Human Recombinant IL-2	StemCell Technologies	78036
RNA Clean & Concentrator 5	Zymo Research	R1013
RNase Inhibitor, Murine	New England Biolabs	M0314S
RPMI 1640 medium	Thermo Fisher Scientific	11875093
SDS (10% w/v)	Fisher Scientific	50-751-7490
SMARTScribe Reverse Transcriptase	Takara	639537
Sodium hydroxide solution (1 N)	Sigma-Aldrich	1091371000
SPRIselect Reagent	Beckman Coulter	B23318
Sterile saline solution injection	Midwest Veterinary Supply	193.74500.3
Sucrose	Sigma-Aldrich	Cat# S0389; CAS# 57-50-1
Temozolamide	Santa Cruz Biotechnology	Cat# sc-203292; CAS# 85622-93-1
Tissue Freezing Medium	General Data	1518313
Trametinib	Santa Cruz Biotechnology	Cat# sc-364639A; CAS# 871700-17-3
Tris (1 M), pH 7.0, RNase-free	Thermo Fisher Scientific	AM9850G
Tris (1 M), pH 8.0, RNase-free	Thermo Fisher Scientific	AM9855G
Triton X-100	Sigma-Aldrich	Cat# T9284; CAS# 9002-93-1
TRIzol reagent	Thermo Fisher Scientific	15596026
TrueBlack Lipofuscin Autofluorescence Quencher	Biotium	23007
Trypan blue stain, 0.4%	Thermo Fisher Scientific	T10282
TWEEN 20	Sigma-Aldrich	Cat# P1379; CAS# 9005-64-5
VECTASHIELD Vibrance Antifade Mounting Medium	Vector Laboratories	H170010
Y-27632	StemCell Technologies	Cat# 72304; CAS# 129830-38-2
Critical Commercial Assays		
Bioanalyzer high sensitivity DNA analysis	Agilent	5067-4626
Click-iT EdU Alexa Fluor 647 Imaging Kit	Thermo Fisher Scientific	C10340
DuoSet ELISA Ancillary Reagent Kit 1	R&D Systems	DY007
EZ-PCR Mycoplasma test kit	Biological Industries	2070020
Human IFN-gamma DuoSet ELISA	R&D Systems	DY285B-05
Human IL-2 DuoSet ELISA	R&D Systems	DY202-05
Human TNF-alpha DuoSet ELISA	R&D Systems	DY210-05
Hypoxyprobe Kit	Hypoxyprobe	HP1-100Kit

REAGENT or RESOURCE	SOURCE	IDENTIFIER
KAPA Library Quantification Kit for Illumina NGS	Kapa Biosystems	KK4835
Neural Tissue Dissociation Kit - Postnatal Neurons	Miltenyi Biotech	130094802
NextSeq High Output v2 150 Cycles	Illumina	TG-160-2002
Qubit dsDNA HS Assay Kit	Thermo Fisher Scientific	Q33231
Quick-DNA Microprep Kit	Zymo Research	D3020
Deposited Data		
Bulk RNA sequencing	This paper	GEO: GSE141947
Whole exome sequencing	This paper	GEO: GSE141947
Single-cell RNA sequencing	This paper	GEO: GSE141947
Single nuclei RNA sequencing of adult human brain	Habib et al., 2017	https://doi.org/10.1038/nmeth.4407
Single nuclei RNA sequencing of adult human brain	Lake et al., 2018	https://doi.org/10.1038/nbt.4038
Experimental Models: Cell Lines		
Glioblastoma organoid samples	This paper	Tables S1 and S2
Experimental Models: Organisms/Strains		
NU/J *Mus musculus*, female	The Jackson Laboratory	Cat# 002019; RRID: IMSR_JAX:002019
Oligonucleotides		
CDS Primer sequence: 5′-AAGCAGTGGTATCAACGCAGAGTACT30VN-3′	IDT	N/A
TSO Primer sequence: 5′-AAGCAGTGGTATCAACGCAGAGTACATrGrGrG-3′	IDT	N/A
LS PCR Primer sequence: 5′-AAGCAGTGGTATCAACGCAGAGT-3′	IDT	N/A
Software and Algorithms		
Adobe Illustrator CC	Adobe	https://www.adobe.com/products/illustrator.html; RRID:SCR_010279
Adobe Photoshop CC	Adobe	https://www.adobe.com/products/photoshop.html; RRID:SCR_014199
ANNOVAR	Wang et al., 2010	http://www.openbioinformatics.org/annovar/; RRID:SCR_012821
avsnp150	Annovar	http://annovar.openbioinformatics.org/en/latest/
bcl2fastq v.2.19.0.316	Illumina	https://support.illumina.com/sequencing/sequencing_software/bcl2fastq-conversion-software.html; RRID:SCR_015058
BWA v.0.7.10	Li and Durbin, 2009	http://bio-bwa.sourceforge.net/; RRID:SCR_010910
COSMIC v88	Sanger	https://cancer.sanger.ac.uk/cancergenome/projects/cosmic/; RRID:SCR_002260
dbNSFP35a	Liu et al., 2016	https://sites.google.com/site/jpopgen/dbNSFP; RRID:SCR_005178
dbSNP b146	Broad Institute	https://www.ncbi.nlm.nih.gov/SNP/; RRID:SCR_002338

REAGENT or RESOURCE	SOURCE	IDENTIFIER
DESeq2 v.1.22.2	Love et al., 2014	https://bioconductor.org/packages/release/bioc/html/DESeq2.html; RRID:SCR_015687
Drop-seq tools v.2.1.0	Saunders et al., 2018	https://github.com/broadinstitute/Drop-seq
Enrichr	Kuleshov et al., 2016	http://amp.pharm.mssm.edu/Enrichr/; RRID:SCR_001575
Freebayes v1.2.0-4-gd15209e	Garrison and Math, 2012	https://github.com/ekg/freebayes; RRID:SCR_010761
GATK v.4.1.0.0	Broad Institute	https://software.broadinstitute.org/gatk/; RRID:SCR_001876
gnomAD	Broad Institute	http://gnomad.broadinstitute.org/; RRID:SCR_014964
GraphPad Prism	GraphPad Software	https://www.graphpad.com/scientific-software/prism/; RRID:SCR_002798
GRCh38 v 28	Genome Reference Consortium	https://www.ncbi.nlm.nih.gov/assembly/GCF_000001405.38
GRCh38 (exome)	Broad Institute	https://software.broadinstitute.org/gatk/documentation/article?id=11010
IGV v2.4.14	Broad Institute	https://www.broadinstitute.org/igv/; RRID:SCR_011793
ImageJ	NIH	https://imagej.nih.gov/ij/; RRID:SCR_003070
Imaris	Bitplane	https://imaris.oxinst.com/packages; RRID:SCR_007370
inferCNV	Broad Institute	https://github.com/broadinstitute/infercnv
Manta v 1.5.0 illumina github	Chen et al., 2016	https://github.com/Illumina/manta
MuTect V4.1.0.0	Broad Institute	https://www.broadinstitute.org/cancer/cga/mutect; RRID:SCR_000559
Picard v. 1.141	Broad Institute	http://broadinstitute.github.io/picard/; RRID:SCR_006525
R Project v.3.5.1	Open source	https://www.r-project.org/; RRID:SCR_001905
RefGenes	Annovar	https://www.refgenes.org/rg/; RRID:SCR_003372
RStudio	Open source	https://rstudio.com/; RRID:SCR_000432
Rsubread v.1.32.2	Liao et al., 2019	https://bioconductor.org/packages/release/bioc/html/Rsubread.html; RRID:SCR_016945
SAMtools/BCFtools v1.9	Li et al., 2009; Li, 2011	http://samtools.sourceforge.net/mpileup.shtml; RRID:SCR_005227
Seurat	Stuart et al., 2019	https://github.com/satijalab/seurat; RRID:SCR_007322
Small ExAX common variants	Broad Institute	http://exac.broadinstitute.org/
STAR v.2.6.1d	Dobin et al., 2013	https://github.com/alexdobin/STAR; RRID:SCR_015899
Strelka v.2.9.10	Kim et al., 2018	https://academic.oup.com/bioinformatics/article-pdf/28/14/1811/16904379/bts271.pdf; RRID:SCR_005109

REAGENT or RESOURCE	SOURCE	IDENTIFIER
SVA v.3.30.1	Leek et al., 2012	https://bioconductor.org/packages/release/bioc/html/sva.html RRID:SCR_002155
VarScan v2.3.9	Koboldt et al., 2012	https://sourceforge.net/projects/varscan/files/ RRID:SCR_006849
Vcflib	GitHub	https://github.com/vcflib/vcflib; RRID:SCR_001231
VCFtools v 0.1.13	Danecek et al., 2011	http://vcftools.sourceforge.net/; RRID:SCR_001235
Zen 2Blue	Carl Zeiss	https://www.zeiss.com/microscopy/us/products/microscope-software/zen-lite.html; RRID:SCR_013672
Other		
Bioanalyzer 2100	Agilent	G2939BA
C&B Metabond Quick Adhesive Cement System Kit	Benco Dental	1681-343
Cell counting slides	Thermo Fisher Scientific	C10228
Countess II Automated Cell Counter	Thermo Fisher Scientific	AMQAX1000
Disposable pellet pestle	Fisher	12-141-368
Fine Forceps - Curved/Serrated	Fine Science Tools	11065-07
Forma Steri-Cult CO2 Incubator	Thermo Fisher Scientific	3310
MACS SmartStrainer, 70 μM	Miltenyi Biotech	130-098-462
MaxQ CO2 Plus Shaker	Thermo Fisher Scientific	88881102
Microfluidic chips for drop-seq	FlowJEM	Custom order
NanoDrop 2000	Thermo Fisher Scientific	ND-2000
NextSeq550	Illumina	SY-415-1002
Pellet pestle cordless motor	Fisher	12-141-361
Qubit 3 Fluorimeter	Thermo Fisher Scientific	Q33216
T100 Thermal Cycler	Bio-rad	1861096EDU
TB Syringe (26 G x 3/8 in, 1 ml)	BD Biosciences	309625
Vannas Spring Scissors - Curved/3mm Cutting Edge	Fine Science Tools	15000-10